A&A 513, A52 (2010)
DOI: 10.1051/0004-6361/200912482
© ESO 2010

Astronomy & Astrophysics

The globular cluster system of NGC 1399⋆,⋆⋆,⋆⋆⋆

V. dynamics of the cluster system out to 80 kpc

Y. Schuberth[1,2], T. Richtler[2], M. Hilker[3], B. Dirsch[2], L. P. Bassino[4], A. J. Romanowsky[5,2], and L. Infante[6]

[1] Argelander-Institut für Astronomie, Universität Bonn, Auf dem Hügel 71, 53121 Bonn, Germany
e-mail: ylva@astro.uni-bonn.de
[2] Universidad de Concepción, Departamento de Astronomia, Casilla 160-C, Concepción, Chile
[3] European Southern Observatory, Karl-Schwarzschild-Str. 2, 85748 Garching, Germany
[4] Facultad de Ciencias Astronómicas y Geofísicas, Universidad Nacional de La Plata, Paseo del Bosque S/N, 1900–La Plata, Argentina; and Instituto de Astrofísica de La Plata (CCT La Plata – CONICET – UNLP)
[5] UCO/Lick Observatory, University of California, Santa Cruz, CA 95064, USA
[6] Departamento de Astronomía y Astrofísica, Pontificia Universidad Católica de Chile, Casilla 306, Santiago 22, Chile

Received 13 May 2009 / Accepted 16 October 2009

ABSTRACT

Globular clusters (GCs) are tracers of the gravitational potential of their host galaxies. Moreover, their kinematic properties may provide clues for understanding the formation of GC systems and their host galaxies. We use the largest set of GC velocities obtained so far of any elliptical galaxy to revise and extend the previous investigations (Richtler et al. 2004) of the dynamics of NGC 1399, the central dominant galaxy of the nearby Fornax cluster of galaxies. The GC velocities are used to study the kinematics, their relation with population properties, and the dark matter halo of NGC 1399. We have obtained 477 new medium-resolution spectra (of these, 292 are spectra from 265 individual GCs, 241 of which are not in the previous data set). with the VLT FORS 2 and Gemini South GMOS multi-object spectrographs. We revise velocities for the old spectra and measure velocities for the new spectra, using the same templates to obtain an homogeneously treated data set. Our entire sample now comprises velocities for almost 700 GCs with projected galactocentric radii between 6 and 100 kpc. In addition, we use velocities of GCs at larger distances published elsewhere. Combining the kinematic data with wide-field photometric Washington data, we study the kinematics of the metal-poor and metal-rich subpopulations. We discuss in detail the velocity dispersions of subsamples and perform spherical Jeans modelling.
The most important results are: the red GCs resemble the stellar field population of NGC 1399 in the region of overlap. The blue GCs behave kinematically more erratic. Both subpopulations are kinematically distinct and do not show a smooth transition. It is not possible to find a common dark halo which reproduces simultaneously the properties of both red and blue GCs. Some velocities of blue GCs are only to be explained by orbits with very large apogalactic distances, thus indicating a contamination with GCs which belong to the entire Fornax cluster rather than to NGC 1399. Also, stripped GCs from nearby elliptical galaxies, particularly NGC 1404, may contaminate the blue sample.
We argue in favour of a scenario in which the majority of the blue cluster population has been accreted during the assembly of the Fornax cluster. The red cluster population shares the dynamical history of the galaxy itself. Therefore we recommend to use a dark halo based on the red GCs alone.
The dark halo which fits best is marginally less massive than the halo quoted previously. The comparison with X-ray analyses is satisfactory in the inner regions, but without showing evidence for a transition from a galaxy to a cluster halo, as suggested by X-ray work.

Key words. galaxies: elliptical and lenticular, cD – galaxies: kinematics and dynamics – galaxies: individual: NGC 1399

1. Introduction

1.1. The globular cluster systems of central elliptical galaxies

Shortly after M 87 revealed its rich globular cluster system (GCS) (Baum 1955; Racine 1968) it became obvious that bright ellipticals in general host globular clusters in much larger numbers than spiral galaxies (Harris & Racine 1979). Moreover, the richest GCSs are found for elliptical galaxies in the centres of galaxy clusters, for which M 87 in the Virgo cluster and NGC 1399 in the Fornax cluster are the nearest examples. For recent reviews of the field, see Brodie & Strader (2006), and Richtler (2006).

The galaxy cluster environment may act in different ways to produce these very populous GCSs. Firstly, there is the paradigm of giant elliptical galaxy formation by the merging of disk

⋆ Based on observations made with ESO Telescopes at the Paranal Observatories under programme ID 70.B-0174.

⋆⋆ Based on observations obtained at the Gemini Observatory, which is operated by the Association of Universities for Research in Astronomy, Inc., under a cooperative agreement with the NSF on behalf of the Gemini partnership: the National Science Foundation (United States), the Particle Physics and Astronomy Research Council (United Kingdom), the National Research Council (Canada), CONICYT (Chile), the Australian Research Council (Australia), CNPq (Brazil) and CONICET (Argentina).

⋆⋆⋆ Tables B.1 and B.2 are only available in electronic form at the CDS via anonymous ftp to cdsarc.u-strasbg.fr (130.79.128.5) or via
http://cdsweb.u-strasbg.fr/cgi-bin/qcat?J/A+A/513/A52

galaxies (e.g. Toomre 1977; Renzini 2006). That early-type galaxies can form through mergers is evident by the identification of merger remnants and many kinematical irregularities in elliptical galaxies (counter-rotating cores, accreted dust and molecular rings).

In fact, starting from the bimodal colour distribution of GCs in some giant ellipticals, Ashman & Zepf (1992) predicted the efficient formation of GCs in spiral-spiral mergers, before this was confirmed observationally (Schweizer & Seitzer 1993). In their scenario, the blue clusters are the metal-poor GCSs of the pre-merger components while the red (metal-rich) GCs are formed in the material which has been enriched in the starbursts accompanying the early merger (gaseous merger model).

However, Forbes et al. (1997) pointed out that the large number of metal-poor GCs found around giant ellipticals cannot be explained by the gaseous merger model. These authors proposed a "multi-phase collapse model" in which the blue GCs are created in a pre-galactic phase along with a relatively low number of metal-poor field stars. The majority of field stars, i.e. the galaxy itself and the red GCs, are then formed from the enriched gas in a secondary star formation epoch. This scenario is also supported by the findings of Spitler et al. (2008) who studied an updated sample of 25 galaxies spanning a large range of masses, morphological types and environments. They confirmed that the spirals generally show a lower fraction of GCs normalised to host galaxy stellar mass than massive ellipticals, thus ruling out the possibility that the GCSs of massive ellipticals are formed through major wet mergers. Further, Spitler et al. suggest that the number of GCs per unit halo mass is constant – thus extending the work by Blakeslee et al. (1997) who found that in the case of central cluster galaxies the number of GCs scales with the cluster mass. These are findings which point towards an early formation of the GCs.

In some scenarios (e.g. Côté et al. 1998; Hilker et al. 1999; Côté et al. 2002; Beasley et al. 2002), the accretion of mostly metal-poor GCs is responsible for the richness of the GCSs of central giant ellipticals.

But only during the last years it has become evident that accretion may be important even for GCSs of galaxies in relatively low density regions like the Milky Way (e.g. Helmi 2008), the most convincing case being the GCs associated with the Sagittarius stream (Ibata et al. 2001; Bellazzini et al. 2003). Therefore, GC accretion should plausibly be an efficient process for the assembly of a GCS in the central regions of galaxy clusters.

Given this scenario one expects huge dark matter halos around central giant ellipticals, perhaps even the sum of a galaxy-size dark halo and a cluster dark halo (e.g. Ikebe et al. 1996). However, dark matter studies in elliptical galaxies using tracers other than X-rays were long hampered by the lack of suitable dynamical tracers. Due to the rapidly declining surface brightness profiles, measurements of stellar kinematics are confined to the inner regions, just marginally probing the radial distances at which dark matter becomes dominant. One notable exception is the case of NGC 6166, the cD galaxy in Abell 2199, for which Kelson et al. (2002) measured the velocity dispersion profile out to a radius of 60 kpc. Another one is the case of NGC 2974 where an HI disk traces the mass out to 20 kpc (Weijmans et al. 2008).

Only with the advent of 8 m-class telescopes and multi-object spectrographs it has become feasible to study the dynamics of globular cluster systems (GCSs) of galaxies as distant as 20 Mpc. Early attempts (Huchra & Brodie 1987; Grillmair et al. 1994; Cohen & Ryzhov 1997; Minniti et al. 1998; Kissler-Patig et al. 1998) were restricted to the very brightest GCs, and even today there are only a handful of galaxies with more than 200 GC velocities measured. Large ($N_{GC} > 200$) samples of GC radial velocities have been published for M 87 (Côté et al. 2001) and NGC 4472 (Côté et al. 2003) in Virgo and NGC 1399 in Fornax (Richtler et al. 2004, hereafter Paper I). Also the GCS dynamics of the nearby (~4 Mpc) disturbed galaxy Cen A (NGC 5128) has been studied extensively (Peng et al. 2004; Woodley et al. 2007), with 340 GC velocities available to date.

Investigating the kinematics and dynamics of GCSs of elliptical galaxies has a twofold objective. Firstly, kinematical information together with the population properties of GCs promise to lead to a deeper insight into the formation history of GCSs with their different GC subpopulations. Secondly, GCs can be used as dynamical tracers for the total mass of a galaxy and thus allow the determination of the dark matter profile, out to large galactocentric distances which are normally inaccessible to studies using the integrated light. These results then can be compared to X-ray studies. A large number of probes is a prerequisite for the analysis of these dynamically hot systems. Therefore, giant ellipticals, known to possess extremely populous and extended GCSs with thousands of clusters, have been the preferred targets of these studies.

Regarding the formation history of GCSs, a clear picture has not yet emerged. Adopting the usual bimodal description of a GCS by the distinction between metal-poor and metal-rich GCs, the kinematical properties seem to differ from galaxy to galaxy. For example, in M 87 the blue and red GCs do not exhibit a significant difference in their velocity dispersion (Côté et al. 2001, with a sample size of 280 GCs). Together with their different surface density profiles, Côté et al. concluded that their orbital properties should be different: the metal-poor GCs have preferentially tangential orbits while the metal-rich GCs prefer more radial orbits.

In NGC 4472, on the other hand, the metal-rich GCs have a significantly lower velocity dispersion than their blue counterparts (found for a sample 250 GCs, Côté et al. 2003), and these authors conclude that the cluster system as a whole has an isotropic orbital distribution.

NGC 1399, the object of our present study, is a galaxy, which, as a central cluster galaxy, is similar to M 87 in many respects (see Dirsch et al. 2003). Here, the metal-poor GCs show a distinctly higher velocity dispersion than the metal-rich GCs, but more or less in agreement with their different density profiles (with a sample size of ~470 GCs). A similar behaviour has been found for NGC 4636 (Schuberth et al. 2006).

In most other studies, the sample sizes are still too small to permit stringent conclusions or the separate treatment of red and blue GCs, but dark matter halos have been found in almost all cases.

1.2. The case of NGC 1399

NGC 1399 has long been known to host a very populous globular cluster system (e.g. Dirsch et al. 2003 and references therein). With the photometric study by Bassino et al. (2006) it became clear that the GCS of NGC 1399 extends to about 250 kpc, which is comparable to the core radius of the cluster (Ferguson & Sandage 1989). Accordingly, it has always been an attractive target for studying the dynamics of its GCS. One finds there the largest sample of GC velocities (469) available so far (Richtler et al. 2004 (Paper I); Dirsch et al. 2004). It was shown in Paper I that blue and red GCs are kinematically different, as was

expected from their different number density profiles: the red GCs exhibit a smaller velocity dispersion than the blue GCs in accordance with their respective density profiles. Evidence for strong anisotropies has not been found. The radial velocity dispersion profile was found to be constant for red and blue GCs. However, as we think now, this could have been a consequence of a velocity cut introduced to avoid outliers. A dark halo of the NFW type under isotropy reproduced the observations satisfactorily. No rotation was detected apart from a slight signal for the outer blue GCs. It was shown that some of the extreme radial velocities in conjunction with the derived dark halo were only understandable if they were being caused by orbits with very large apogalactic distances. In this paper, we extend our investigation of the NGC 1399 GCS to larger radii (80 kpc). We simultaneously revise the old velocities/spectra in order to have an homogeneously treated sample. The case of Modified Newtonian Dynamics (MOND) has already been discussed in Richtler et al. (2008), where it has been shown that MOND still needs additional dark matter of the order of the stellar mass. We do not come back to this issue in the present contribution.

The GCS of NGC 1399 is very extended. One can trace the blue GCs out to about 250 kpc, the red GCs only to 140 kpc (Bassino et al. 2006). Regarding total numbers, there are only half as many red GCs as there are blue, suggesting that the formation of GCs in mergers is not the dominant mechanism producing a high specific frequency, even if in the central regions of a proto-cluster the merger rate is supposed to be particularly high.

Following Paper I, we assume a distance modulus of 31.40. At the distance of 19 Mpc, 1″ corresponds to 92 pc, and 1′ corresponds to 5.5 kpc.

This paper is organised as follows: in Sect. 2, we describe the observations and the data reduction. The velocity data base is presented in Sect. 3. In Sect. 4, we present the photometric properties and the spatial distribution of our GC velocity sample. The contamination by interlopers is discussed in Sect. 5. The properties of the line-of-sight velocity distribution are studied in Sect. 6. In Sect. 7 we test our GC sample for rotation. The line-of-sight velocity dispersion and the higher order moments of the velocity distributions are calculated in Sect. 8. The Jeans modelling and the derived mass models are described in Sects. 9 and 10. The results are discussed and summarised in Sects. 11 and 12.

2. Observations and data reduction

To study the dynamics of the GCS of NGC 1399 out to large radii, we use data obtained with the multi-object-spectrographs FORS2/MXU and GMOS-S, at the VLT and Gemini-South telescopes, respectively. The spectral resolution and wavelength coverage is similar for both datasets. Details on the mask preparation and data reduction are given below.

The location of the GCs on the plane of the sky is shown in Fig. 1. The GCs from Paper I (shown as dots) occupy the inner region, and open symbols represent the GCs added in the present study, raising the number of GC velocities to almost 700 and extending the radial range by almost a factor of two.

2.1. Photometric data

Wide-field imaging in the metallicity-sensitive Washington system obtained for several fields in the Fornax cluster using the CTIO MOSAIC camera[1] forms the basis for the photometry used in this work. The central field (Dirsch et al. 2003) encompasses the area covered by our spectroscopic study. As in Paper I, these data were used for target selection, and the photometric properties of our velocity-confirmed GCs are presented in Sect. 4.1.

Further, the analysis of the outer fields presented by Bassino et al. (2006) provides the number density profiles of the GC subpopulations out to large radii (cf. Sect. 9.2) which are required for the dynamical modelling.

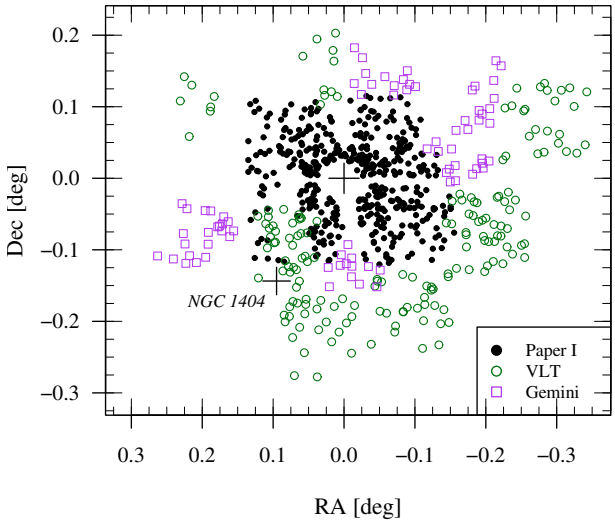

Fig. 1. Spatial distribution of spectroscopically confirmed GCs with respect to NGC 1399 (0, 0). Dots represent GCs from Paper I. Circles and squares are the new GCs, measured using VLT/FORS 2 and Gemini/GMOS, respectively. *North is to the top and East is to the left.* The positions of NGC 1399 and NGC 1404 are marked by crosses.

2.2. VLT-FORS2/MXU spectroscopy

The spectroscopic observations of 11 masks in seven fields (see Table 1 for details) were carried out in visitor mode during three nights (2002 December 1−3) at the European Southern Observatory Very Large Telescope (VLT) facility on Cerro Paranal, Chile. We used the FORS 2 (Focal Reducer/low dispersion Spectrograph) instrument equipped with the Mask Exchange Unit (MXU).

Our spectroscopic targets were selected from the wide-field photometry by Dirsch et al. (2003, hereafter D+03). The masks were designed using the FIMS software. To maximise the number of objects per mask, we observed objects and sky positions through separate slits of 2″ length. This strategy has previously been used for the study of NGC 1399 (Dirsch et al. 2004, D+04 hereafter) and NGC 4636 (Schuberth et al. 2006).

All observations were performed using the grism 600 B which provides a spectral resolution of ∼2.5 Å ≃ 150 km s^{-1} (as measured from the line-widths of the wavelength calibration exposures).

The reduction of the FORS2/MXU spectra was performed in the same way as described in Dirsch et al. (2004), so we just give a brief description here. After the basic reduction steps (bias subtraction, flat fielding, and trimming), the science and calibration frames were processed using the `apextract`

[1] The camera is mounted in the prime focus of the 4-m Blanco telescope and the field-of-view is 36′ × 36′.

Table 1. Summary of VLT FORS 2/MXU observations (programme ID 70.B-0174).

Mask	ID	Centre position (J 2000)		Exp. time (s)	Seeing	# Slits	# GCs	Night
Mask 1	965 705	03:37:15.9	−35:22:18.2	2600	0.″90	130	9	2002-12-01
Mask 2	965 813	03:37:22.1	−35:22:18.5	2600	0.″90	132	16	...
Mask 3	965 930	03:37:34.7	−35:31:40.9	2600	0.″65	130	24	...
Mask 4	970 048	03:37:40.9	−35:31:41.9	2600	0.″75	132	27	...
Mask 5	970 253	03:38:02.8	−35:38:15.7	2600	0.″85	131	21	...
Mask 7	971 436	03:38:48.4	−35:32:53.6	2600	0.″80	128	36	2002-12-02
Mask 8	973 401	03:39:21.8	−35:21:27.2	2600	0.″65	127	7	...
Mask 9	970 843	03:38:33.4	−35:40:34.1	2600	0.″85	122	9	...
Mask 10	971 105	03:38:39.6	−35:40:35.3	2600	0.″80	124	18	...
Mask 12	970 540	03:38:09.1	−35:38:14.6	2600	1.″35	129	12	...
Mask 13	972 414	03:38:40.5	−35:17:24.9	2600	1.″45	127	10	2002-12-03

Notes. The six-digit number given in the second column is the mask identifier as given in the image header (keyword: `HIERARCH ESO INS MASK ID`). The seeing values (Col. 6) were determined from the acquisition images taken just before the MXU exposures. The numbers given in Cols. 7 and 8 refer to the total number of slits and the number of GCs found on a given mask, respectively.

Table 2. Summary of Gemini South GMOS observations (program IDs GS 2003B Q031 and GS 2004B Q029).

Mask	Centre position (J 2000)		Exp. Time (s)	Seeing	# Slits	# GCs	Night
m2003-01	03:39:20.2	−35:31:58.6	2600	0.″58	31	14	2003-11-19
m2003-02	03:39:20.2	−35:31:58.6	3900	0.″80	21	8	2003-11-20
m2003-03	03:38:13.4	−35:18:03.0	3900	0.″73	27	7	2003-11-23 ⋆
m2003-04	03:38:13.4	−35:18:03.0	3900	0.″55	24	3	2003-11-23 †
m2004-01	03:38:13.4	−35:18:03.0	2600	0.″66	27	8	2004-12-07 ⋆
m2004-02	03:38:13.4	−35:18:03.0	3900	0.″70	24	4	2004-12-07 †
m2004-03	03:37:44.9	−35:19:06.2	3900	0.″57	30	10	2004-12-10
m2004-04	03:37:44.9	−35:19:06.2	3900	0.″73	21	1	2004-12-10
m2004-05	03:37:46.0	−35:24:41.1	3900	0.″50	31	14	2004-12-11
m2004-06	03:37:46.0	−35:24:41.1	3900	0.″58	25	5	2004-12-11
m2004-07	03:38:22.8	−35:34:59.2	3900	0.″58	30	18	2004-12-12
m2004-08	03:38:22.8	−35:34:59.2	3900	0.″70	25	5	2004-12-12

See Fig. 5 for a comparison of the velocity measurements.

Notes. (⋆) The masks m2003-03 and m2004-01 are identical; (†) m2003-04 and m2004-02 are identical. The seeing (Col. 5) as estimated from the 2D-spectra of bright stars. The number of slits and the number of GCs detected on a given mask are given in Cols. 6 and 7, respectively.

package in IRAF. The wavelength calibration was performed using `identify`. Typically 18 lines of the Hg-Cd-He arc lamp were used to fit the dispersion relation, and the residuals were of the order 0.04 Å. To perform the sky subtraction for a given GC-spectrum, the spectra of two or three nearby sky-slits were averaged and subsequently subtracted using the `skytweak` task.

2.3. Gemini GMOS spectroscopy

We used the Gemini Multi-Object Spectrograph (GMOS) on Gemini-South, and the observations were carried out in queue mode in November 2003 and December 2004. A total of ten spectroscopic masks in five fields were observed. Table 2 summarises the observations. The mask layout was defined using the GMOS Mask Design software. Again, we selected the GC candidates from the D+03 photometry. We chose slits of 1″ width and 5″ length. We used the B600+_G5323 grating, centred on 5500 Å, giving a resolution of 0.9 Å per (binned) pixel. The spectral resolution is ∼4.5 Å.

The GMOS field of view is 5.′5 × 5.′5, and the detector array consists of three 2048 × 4608 CCDs arranged in a row (2 × 2 binning results in a pixel scale of 0.″146 pixel^{-1}). Thus, with the chip gaps being perpendicular to the dispersion direction, two gaps show up in the spectra. For each mask, the observations typically consisted of three consecutive 1300 s exposures, which were bracketed by exposures of a CuAr arc lamp and screen flat exposures.

The data were reduced using version 1.6 of the `gemini.gmos` IRAF-package in conjunction with a number of customised scripts. The two prominent "bad columns" on the CCD-mosaic were corrected for using `fixpix`, with the interpolation restricted to the dispersion direction. Cosmic ray (CR) rejection was done by combining the science exposures using `gemcombine` with the CR rejection option. The wavelength calibration was performed using `gswavelength`: Chebyshev polynomials of the 4th order were used to fit the dispersion relation. The number of lines used in these fits varied depending on the location of the slit, but typically ∼70 lines were identified, and the residuals (rms) were of the order 0.15 Å. We carefully inspected all calibration spectra in order to exclude blended lines and lines in the proximity of the chip gaps. In the next step, the wavelength calibration was applied

to the science spectra using `gstransform`. The sky subtraction was done using the source-free regions of the slit, by using the `gsskysub` task in interactive mode. The final one-dimensional spectra were extracted using `gsextract`: the apertures were typically 1″ wide, and the tracing was done using Chebyshev polynomials of the 4th−8th order.

3. The velocity data base

In this section, we detail how we build our velocity data base. The radial velocities are measured using Fourier-cross-correlation. Coordinates, colours and magnitudes are taken from the D+03 Washington photometry. We anticipate here that we adopt $C-R = 1.55$ to divide blue (metal-poor) from red (metal-rich) GCs (cf. Sect. 4.1), and the division between foreground stars and bona-fide GCs is made at $v = 450\,\mathrm{km\,s^{-1}}$ (cf. Sect. 3.7).

To obtain a homogeneous data set, we also re-measure the velocities for the spectra used in Paper I (the velocities are tabulated in D+04).

3.1. Radial velocity measurements

The radial velocities are obtained using the IRAF-`fxcor` task, which implements the Fourier cross-correlation technique by Tonry & Davis (1979). The templates (i.e. reference spectra) are the FORS 2/MXU spectrum of NGC 1396 ($v = 815 \pm 8\,\mathrm{km\,s^{-1}}$), which was already used by D+04, and the spectrum of a bright GC in the NGC 4636 GCS[2]. The latter has a heliocentric velocity of $980 \pm 15\,\mathrm{km\,s^{-1}}$, its colour is $C-R = 1.62$ and the R-magnitude is 19.9. Since the spectral resolution for both datasets is similar, we use these templates for the FORS 2/MXU as well as the GMOS data.

The cross-correlation is performed on the wavelength interval $4200 \lesssim \lambda \lesssim 5500$ Å. The upper bound excludes sky-subtraction residuals from the most prominent telluric emission line at 5577 Å, and the lower bound ensures that we are well within the region for which the FORS 2 wavelength calibration is reliable. For the GMOS data, we did not interpolate over the chip gaps. Hence these features are easily identified and excluded from the spectral regions used for the cross-correlation.

Our spectral database contains velocities for 1036 spectra where we could identify a clear peak in the cross-correlation function (CCF). This number does not include obviously redshifted background galaxies.

For each spectrum, we adopt as velocity the `fxcor` measurement with the highest value of the quality parameter $\mathcal{R}_{\mathrm{TD}}$ (which is inversely proportional to the velocity uncertainty Δv, see Tonry & Davis 1979 for details). For 973 spectra, both templates yielded a velocity measurement. For the remaining 63 spectra, only one of the templates returned a robust result.

3.2. Velocity uncertainties of the GCs

The left panel of Fig. 2 shows the velocity uncertainties (as computed by `fxcor`) for the GCs as a function of R-magnitude. As expected, the fainter GCs have larger velocity uncertainties. Red and blue GCs show the same trend, yet the offset between the median values shows that the blue GCs, on average, have larger velocity uncertainties.

[2] This spectrum is part of the dataset analysed in Schuberth et al. (2009, in prep.).

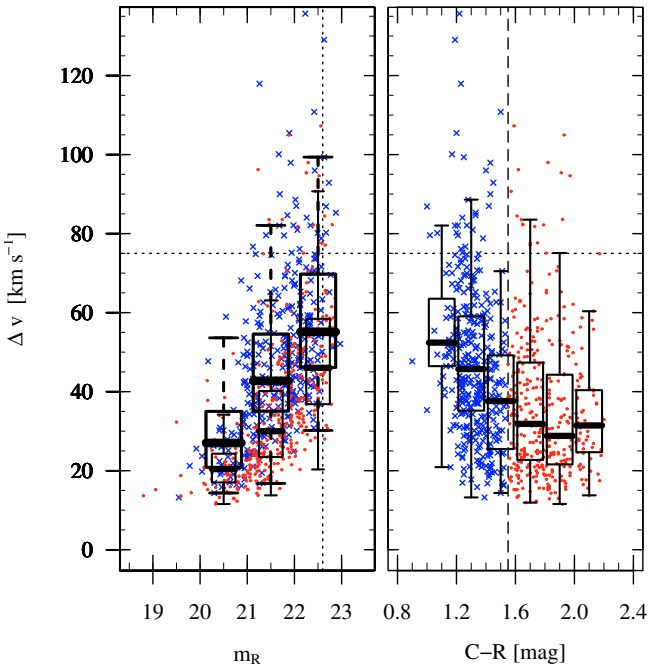

Fig. 2. Velocity uncertainties of the GC spectra as computed by `fxcor`. In both panels, crosses and dots represent blue and red GCs, respectively. *Left panel*: `fxcor`-uncertainties versus R-magnitude. Narrow and wide box-plots show the data for red and blue GCs, respectively. *Right panel*: `fxcor`-uncertainties vs. $C-R$ colour overlaid with box-plots. The long-dashed line at $C-R = 1.55$ shows the division between blue and red GCs. In both panels, the short-dashed lines show the cuts used for assigning the quality flags (cf. Sect. 3.3). The boxes show the interquartile range (IQR), with the band marking the median. The whiskers extend to 1.5 times the IQR or the outermost data point, if closer.

The right panel shows the uncertainties versus $C-R$ colour. One indeed finds that the uncertainties increase as the GCs become bluer. While this might partly be due to template mismatching, the paucity of absorption features in the spectra of the metal-poor GCs by itself leads to larger uncertainties. We compared the velocity measurements of some of the bluest objects using the spectrum of a bright blue GC as template and did not find any significant difference in the derived velocities or uncertainties compared to the results obtained with the other templates.

3.3. Quality flags

Given that our spectroscopic targets have R-magnitudes in the range $18.80 \le m_R \le 22.97$, the accuracy of the velocity determinations varies strongly, as illustrated in the left panel of Fig. 2. With decreasing S/N, the risk of confusing a prominent random peak of the CCF with the "true" peak of the function increases. With the goal of weeding out spurious and probably inaccurate velocity determinations, we therefore assign quality flags (Class A or B) to the spectra: if at least one of the criteria listed below is fulfilled, the velocity measurement is regarded as "uncertain" and the corresponding spectrum is flagged as "Class B":

- only one template yields a velocity measurement;
- velocities measured with the two templates deviate by more than $50\,\mathrm{km\,s^{-1}}$;
- velocity uncertainty $\Delta v \ge 75\,\mathrm{km\,s^{-1}}$;
- quality parameter $\mathcal{R}_{\mathrm{TD}} \le 4.5$;
- relative height of the CCF peak $\mathrm{HGHT_{corr}} < 0.15$;

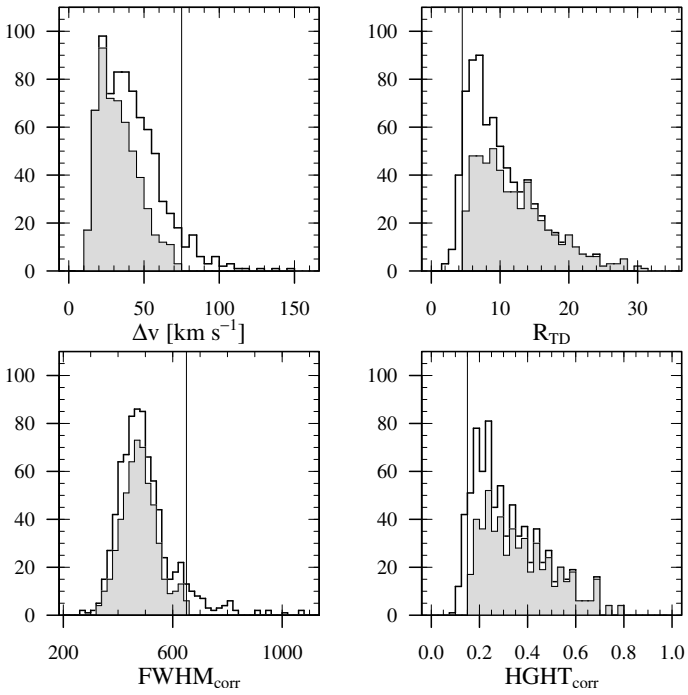

Fig. 3. `fxcor` parameters and data classification. The panels show the histograms for all (unfilled histograms) and the "Class A" (grey histogram bars) GC spectra. *Top left*: velocity uncertainty, cut at 75 km s^{-1}. *Top right*: $\mathcal{R}_{TD}$, the cut is at 4.5. *Bottom left*: *FWHM* of the fitted cross-correlation peak, the cut is at 650 km s^{-1}. *Bottom right*: relative height of the cross-correlation peak, the cut is at 0.15. In all panels, the vertical line shows the corresponding cut.

- width of the CCF peak $FWHM_{corr} \geq 650$ km s^{-1};
- R-magnitude limit: $m_R \geq 22.6$.

Figure 3 shows the distribution of the `fxcor` parameters for all GC spectra as unfilled histograms. In each sub-panel, the vertical line indicates the respective value defining the "Class B" (uncertain) measurements. The "Class A" spectra are shown as grey histograms.

Assigning these quality flags to the spectra yields 723 Class A and 313 Class B measurements.

3.4. The new spectra

For the new data set, velocities were determined for 477 spectra, 179 (139) of which were obtained with GMOS, and 298 (200) with FORS 2, where the numbers in brackets refer to the Class A measurements. The slightly higher fraction of Class A spectra found for the GMOS data is probably due to the different treatment of the sky which, for the GMOS data, was subtracted prior to the extraction.

3.5. Re-measuring the spectra from Paper I

Our re-analysis of the spectral data set from Paper I yielded 559 `fxcor` velocities (GCs and foreground stars). Our database and the D+04 catalogues have 503 (GCs and foreground stars) spectra in common, and the results are compared below.

The GC catalogue by D+04 (their Table 3) lists the velocities[3] for 502 GC spectra, and the authors quote 468 as the number of individual GCs. This number drops to 452 after accounting for doubles overlooked in the published list.

We determine `fxcor` velocities for 455 (of the 502) spectra, which belong to 415 individual GCs. With a median R-magnitude of 22.5, the 47 spectra for which no unambiguous `fxcor` velocity measurement could be achieved belong to the fainter objects in our data set.

The difference between our measurements and the values presented in Table 3 of D+04 are plotted against the R-magnitude in the upper panel of Fig. 4. For most spectra, the agreement is very good, but a couple of objects show disturbingly large discrepancies. For faint objects, deviations of the order several hundred km s^{-1} are possibly due to multiple peaks in the CCF which occur in low S/N-spectra.

However, we also find very large (>200 km s^{-1}) differences for seven "Class A" spectra (marked with squares in Fig. 4). Of these GCs, one is also present on a second mask: object 90:2 (the labelled object at $v = 1688 \pm 31$, $v_{D04} = 817 \pm 27$ km s^{-1}) was observed with GMOS (spectrum GS04-M07:171, $v = 1710 \pm 34$ km s^{-1}), thus confirming our new measurement. The remaining six spectra (in order of decreasing brightness: 86:19, 75:9, 90:2, 77:84, 78:102, 81:5, 75:24, and 86:114), and the spectrum 81:55 (for which no photometry is available) are re-classified as "Class B".

Since, for three of the very discrepant spectra (75:9, 78:102, and 90:2), the line-measurements (v_ℓ) by D+04 lie within just 75 km s^{-1} of our new values, we suspect that, in some cases, typographical errors in the published catalogue might be the cause of the deviations.

Table 4 in D+04 lists the velocities for 72 spectra[4] of foreground stars with velocities in the range $-350 \leq v_c \leq 320$ km s^{-1}. Our data base contains measurements for 48 of these spectra (44 objects). The overall agreement is good, but objects 77:6 and 91:82 show large >1000 km s^{-1} deviations and are re-classified as GCs (spectra of Class B). For the remaining spectra, the velocity differences are of the order of the uncertainties

Finally, our database contains velocities for 56 (55 objects) spectra (eleven are foreground stars and 45 (44) GCs) that do not appear in the lists of D+04.

The reason for this discrepancy is unknown.

3.6. Duplicate measurements

In this section, we use the duplicate measurements to assess the quality and robustness of our velocity determinations. First, we compare the velocities obtained when exposing the same mask on two different occasions. Secondly, we have objects which are present on more than one spectroscopic mask (but the instrument is the same). Then, we compare the results for objects observed with both FORS 2 and GMOS. Finally, we compare common objects to values found in the literature where a different instrument (FLAMES) was used.

3.6.1. Double exposures of GMOS masks

For the GMOS dataset, two masks (marked by an asterisk/dagger in Table 2) were exposed during both observing campaigns. As can be seen from the upper left panel of Fig. 5 where we plot the

[3] These authors give two velocities per spectrum, v_c is the value derived with `fxcor`, and v_ℓ refers to the direct line measurement (`rvidlines`).

[4] The entry for 80:99 is a duplicate of 80:100. The object in slit 80:99 is a GC listed in Table 3 of D+04.

Table 3. Descriptive statistics of the line-of-sight velocity distribution.

ID	N_{GC}	$\langle v \rangle$	sd	σ_{los}	Skew	κ	p_{AD}	p_{KS}	p_{SW}
(1)	(2)	(3)	(4)	(5)	(6)	(7)	(8)	(9)	(10)
No colour selection, no magnitude limit									
AI	693	1457 ± 12	312	309 ± 9	–0.16 ± 0.09	0.12 ± 0.15	0.10	0.08	0.10
AII	670	1446 ± 12	306	302 ± 9	–0.18 ± 0.09	0.21 ± 0.16	0.07	0.07	0.08
AV	729	1438 ± 11	294	290 ± 8	–0.33 ± 0.08	0.16 ± 0.16	0.01	0.06	0.01
Faint (m_R < 21.1) GCs, no colour selection									
FII	493	1449 ± 14	309	304 ± 10	–0.07 ± 0.10	0.12 ± 0.17	0.45	0.46	0.69
FIV	297	1432 ± 17	288	285 ± 12	–0.23 ± 0.11	–0.07 ± 0.18	0.28	0.37	0.14
Bright (m_R < 21.1) GCs									
BRI	144	1435 ± 25	307	305 ± 18	–0.50 ± 0.18	0.44 ± 0.39	0.05	0.03	0.02
BRII	140	1428 ± 25	294	292 ± 18	–0.59 ± 0.20	0.61 ± 0.45	0.03	0.03	0.01
BRIII	137	1424 ± 24	280	279 ± 17	–0.67 ± 0.21	0.72 ± 0.53	0.02	0.04	0.01
BRIV	127	1412 ± 25	283	282 ± 18	–0.63 ± 0.22	0.67 ± 0.52	0.03	0.02	0.01
Blue GCs ($m_R \geq 21.1$)									
BI	256	1452 ± 23	362	358 ± 16	–0.06 ± 0.12	–0.35 ± 0.17	0.65	0.50	0.67
BII	246	1435 ± 23	356	351 ± 16	–0.04 ± 0.12	–0.27 ± 0.18	0.72	0.55	0.81
BIII	240	1415 ± 22	337	333 ± 16	–0.21 ± 0.11	–0.42 ± 0.16	0.22	0.14	0.09
BIV	139	1426 ± 29	338	334 ± 20	–0.27 ± 0.14	–0.49 ± 0.20	0.10	0.06	0.07
BV	336	1420 ± 17	316	312 ± 12	–0.3 ± 0.11	–0.14 ± 0.17	0.18	0.39	0.05
Red GCs ($m_R \geq 21.1$)									
RI	256	1472 ± 16	259	256 ± 12	0.02 ± 0.14	0.02 ± 0.21	0.48	0.70	0.70
RII	247	1463 ± 16	254	251 ± 12	0.02 ± 0.14	0.09 ± 0.22	0.37	0.60	0.63
RIII	243	1463 ± 16	242	239 ± 11	0.04 ± 0.13	–0.08 ± 0.20	0.55	0.80	0.66
RIV	158	1437 ± 19	238	234 ± 13	–0.02 ± 0.14	–0.14 ± 0.25	0.80	0.63	0.76
RV	329	1453 ± 14	254	251 ± 10	-0.2 ± 0.15	0.33 ± 0.36	0.24	0.09	0.12

Notes. This table summarise the basic statistical properties for the velocity samples defined in Sect. 5.4. The samples are identified in the first column while the second column gives the corresponding number of GC velocities. Column 3 lists the mean velocity, and the standard deviation is given Col. 4. The dispersion σ_{los}, as returned by the Pryor & Meylan (1993) estimator, is given in Col. 5. The third and fourth moments of the velocity distributions, the skewness and the (reduced) kurtosis κ, are listed in Cols. 6 and 7, respectively, and the uncertainties were estimated using bootstrap resampling. Columns 8 through 10 give the p-values returned by the Anderson-Darling, Lilliefors (Kolmogorov-Smirnov), and the Shapiro-Wilks (W-test) test for normality, respectively. The Roman numerals refer to the sequence of subsamples defined in Sect. 5.4, where (I) is the full sample, prior to interloper removal. (II): GCs within 3′ of NGC 1404 removed, (III): extreme velocities removed via TME algorithm (Sect. 5.3); (IV): restriction to Class A velocity measurements, and (V) includes the data from B+07.

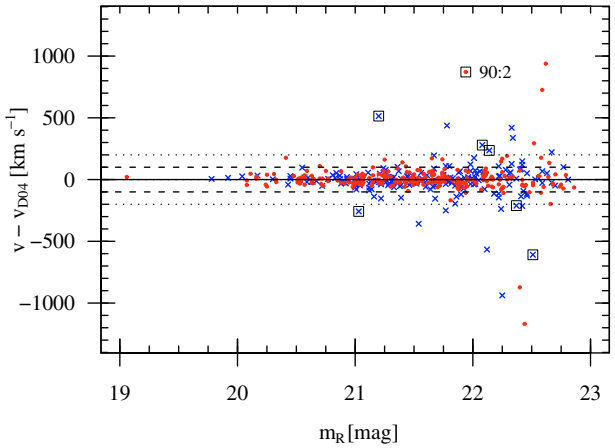

Fig. 4. Comparison to the velocity measurements by Dirsch et al. (2004). Velocity difference vs. R-magnitude. Dots and crosses represent red and blue GCs, respectively. The dashed (dotted) lines are drawn at ±100 (±200) km s^{-1}. The squares indicate the spectra with a large (>200 km s^{-1}) deviations but a "Class A" velocity determination according to the criteria given in Sect. 3.3, and the label refers to the object 90:2 for which a second spectrum exists (see text for details).

velocity differences versus the R-magnitude, the velocities agree fairly well within the uncertainties. The offset of 10 km s^{-1} is negligible and the rms is about 55 km s^{-1}.

3.6.2. Objects observed on different FORS 2 masks

The upper right panel of Fig. 5 compares the velocities measured for 82 objects present on different FORS 2 masks. The agreement is good, and the differences are compatible with the velocity uncertainties. The two outliers, GCs with deviations of the order 300 km s^{-1} (objects 89:92 = 90:94, m_R = 21.43 mag, and 81:8 = 82:22, m_R = 21.0 mag) are both from the data set analysed in Paper I. Also in Table 3 of D+04, the correlation velocities of these objects differ significantly (by 153 and 369 km s^{-1}, respectively). We therefore assign these objects (which nominally have "Class A" spectra) to Class B.

3.6.3. GMOS and FORS 2 spectra

There are 15 objects which were measured with both FORS 2 and GMOS. All of them are GCs, and for all but two photometry is available. The bottom left panel of Fig. 5 shows the velocity differences against the R-magnitude. The offset of ≈10 km s^{-1} is negligible, and the rms is ≈70 km s^{-1}.

3.6.4. The measurements by Bergond et al. (2007)

Bergond et al. (2007, B+07 hereafter) used the FLAMES fibre-spectrograph on the VLT to obtain very accurate ($\Delta v \sim$ 10 km s^{-1}) velocities for 149 bright GCs in the Fornax cluster. Of these objects, 24 (21 of which have Washington photometry) were also targeted in this study, and the velocities are

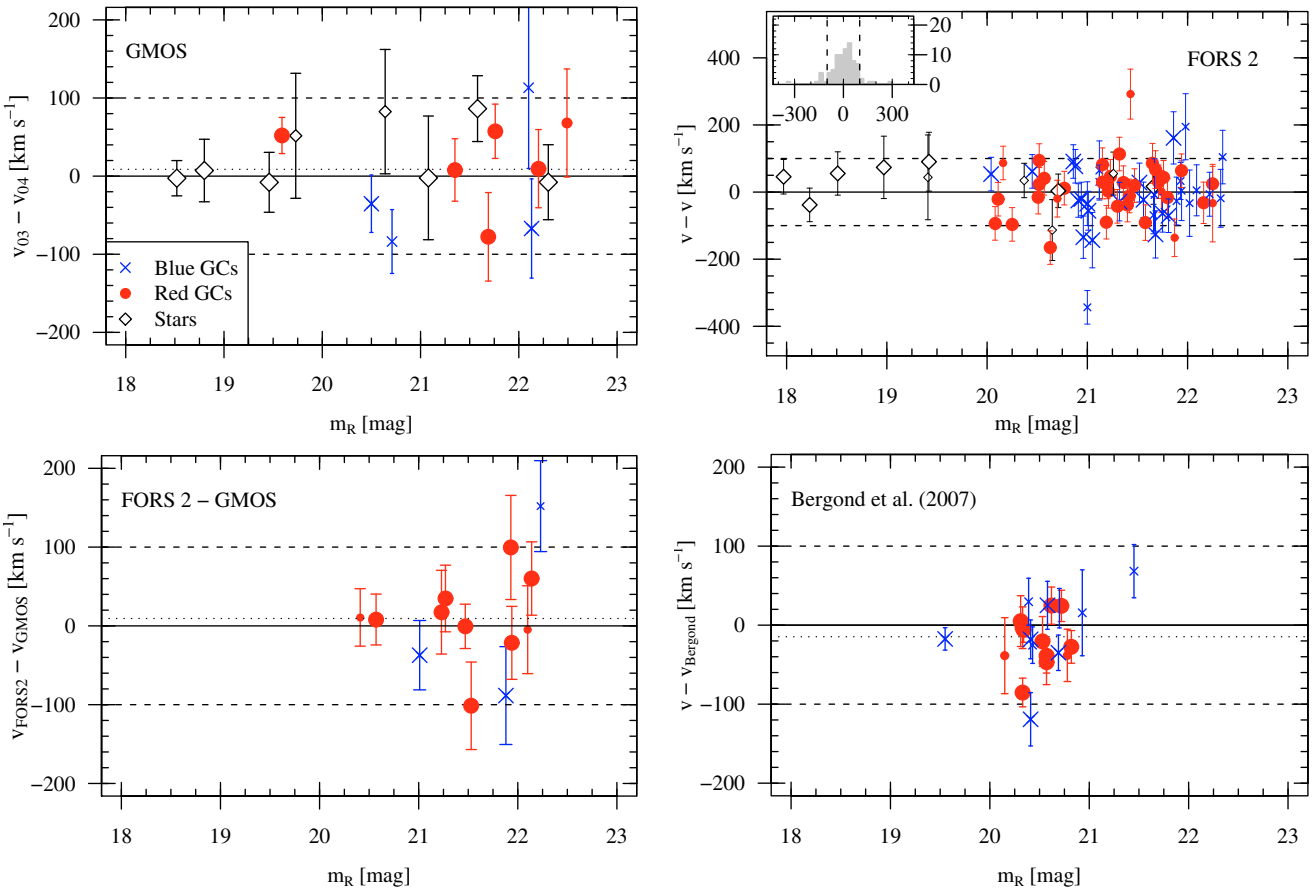

Fig. 5. Duplicate measurements: velocity differences vs. apparent magnitude. Crosses and dots are blue and red GCs, respectively. Foreground stars are shown as diamonds. The error-bars are the uncertainties of the two velocity measurements added in quadrature. Small symbols indicate objects where at least one of the spectra is classified as "Class B". In all panels, the dashed lines are drawn at $\pm 100\,\mathrm{km\,s^{-1}}$. *Upper left*: the GMOS observations labelled in Table 2 (⋆, †) were carried out using the same masks. The scatter (rms $\approx 55\,\mathrm{km\,s^{-1}}$) is of the order of the velocity uncertainties, and the offset, which is $\sim 10\,\mathrm{km\,s^{-1}}$ (dotted line), is very small. *Upper right*: FORS 2 data comparison: difference between the velocities measured for common objects on different masks. The inset shows the histogram of the deviations, which follow a normal distribution with $\sigma \simeq 70\,\mathrm{km\,s^{-1}}$. The two outliers with deviations of $\approx 300\,\mathrm{km\,s^{-1}}$ are re-classified as Class B (see text for details). *Bottom left*: the same for objects measured using both GMOS and VLT. The offset is small ($\sim 10\,\mathrm{km\,s^{-1}}$), and the rms is $\approx 70\,\mathrm{km\,s^{-1}}$. *Bottom right*: comparison to the FLAMES velocity measurements by Bergond et al. (2007). The error-bars show the uncertainties of our and their velocity measurements added in quadrature. The scatter is small (rms = $41\,\mathrm{km\,s^{-1}}$), and the offset, which is $-15\,\mathrm{km\,s^{-1}}$ (dotted line), is negligible.

compared in the bottom right panel of Fig. 5. The offset is $\approx 15\,\mathrm{km\,s^{-1}}$, and the rms is $\approx 40\,\mathrm{km\,s^{-1}}$. With the exception of two outliers (9:71 = gc216.7, 9:43 = gc.154.7), the agreement is excellent. The reason for the deviation of these two objects remains unknown.

3.6.5. Accuracy and final velocities

The repeat measurements of two GMOS masks shows that our results are reproducible. The absence of systematic differences/offsets between the different spectrographs indicates that the instrumental effects are small.

For the GCs for which duplicate measurements exist, we list as final velocity the mean of the respective Class A measurements (using the $\mathcal{R}_{TD}$ values as weights). In case all spectra were classified as Class B, the weighted mean of these velocities is used.

3.7. Separating GCs from foreground stars

To separate GCs from foreground stars we plot, in the upper panel of Fig. 6, colours versus heliocentric velocity. The data points fall into two regions: the highest concentration of objects is found near the systemic velocity of NGC 1399 ($1441 \pm 9\,\mathrm{km\,s^{-1}}$, Paper I). These are the GCs, and we note that all of them have colours well within the interval used by D+03 to identify GC candidates (horizontal dashed lines). The second group of objects, galactic foreground stars, is concentrated towards zero velocity and occupies a much larger colour range[5]. The velocity histograms shown in the lower panel of Fig. 6 illustrate that the total sample, including those objects for which no photometry is available (unfilled histogram), exhibits the same velocity structure as the one found for the objects with MOSAIC photometry (grey histogram). Most importantly, the domains of GCs and foreground stars are separated by a gap of $\sim 100\,\mathrm{km\,s^{-1}}$. Guided by Fig. 6, we therefore regard all objects within the velocity range $450 < v_{helio} < 2500\,\mathrm{km\,s^{-1}}$ as bona fide NGC 1399 GCs.

[5] The data set includes foreground stars which do not fulfil the colour criteria for GC candidates because we extracted all spectra of a given mask, including those from the "positioning slits" used for the MXU mask alignment.

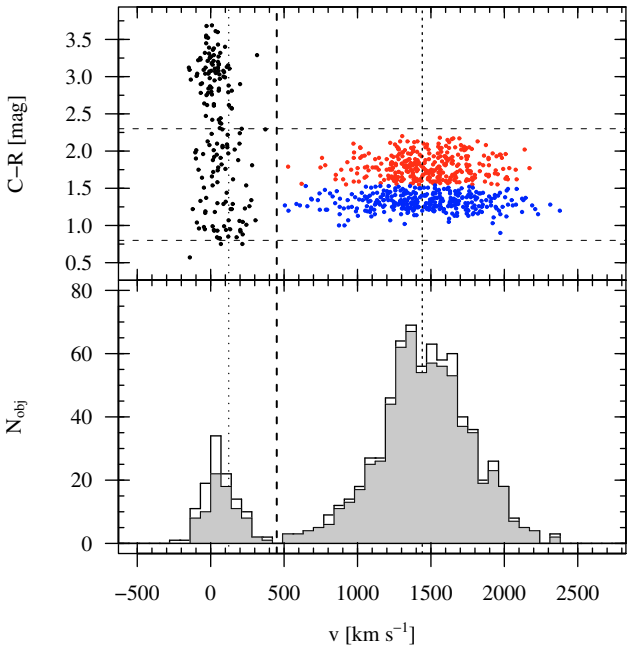

Fig. 6. Separating GCs from foreground stars: *Upper panel*: $C - R$ colour vs. heliocentric velocity for objects with velocities in the range $-500 < v < 3000\,\mathrm{km\,s^{-1}}$. The dashed lines at $C - R = 0.8$ and 2.3 show the colour interval D+03 used to define GC candidates. *Lower panel*: the grey histogram shows the velocities of the objects within the above colour interval. The unfilled histogram also includes those objects for which no photometry is available. In both plots, the short-dashed vertical line at $1441\,\mathrm{km\,s^{-1}}$ indicates the systemic velocity of NGC 1399. The Galactic foreground stars have a mean velocity of about $50\,\mathrm{km\,s^{-1}}$ and exhibit a larger range in colours. The dotted line shows the GSR velocity vector in the direction of Fornax ($124\,\mathrm{km\,s^{-1}}$). The dashed line at $450\,\mathrm{km\,s^{-1}}$ indicates the limit adopted to separate GCs from foreground stars.

3.8. The final velocity catalogue

We determined `fxcor` velocities for a total of 1036 spectra. These objects are foreground stars and GCs. Background galaxies were discarded at an earlier stage of the data analysis, and there were no ambiguous cases, since there is a substantial velocity gap behind the Fornax cluster (Drinkwater et al. 2001).

Our final velocity catalogue comprises 908 unique objects, 830 of which have MOSAIC photometry. This database contains 693 (656 with photometry) GCs, 210 (174 with photometry) foreground stars and five Fornax galaxies (NGC 1404, NGC 1396, FCC 208, FCC 222, and FCC 1241). Of the GCs, 471 have velocities classified as Class A, the remaining 222 have Class B measurements. The velocities for the GCs and the foreground stars are available in electronic form (Tables B.1 and B.2 for GCs and stars, respectively). For each spectrum, the tables give the coordinates, the `fxcor`-velocity measurement, the $\mathcal{R}_{\mathrm{TD}}$-parameter, and the quality flag. The final velocities and the cross-identifications are also given.

4. Properties of the globular cluster sample

4.1. Colour and luminosity distributions

The luminosity distribution of our GC sample is plotted in the upper left panel of Fig. 7. The turn-over magnitude (TOM) of $m_R = 23.3$ (D+03) is shown for reference. It illustrates that our spectroscopic study only probes the bright part of the globular cluster luminosity function (GCLF). The distributions for red and blue GCs, shown as kernel density estimates (e.g. Venables & Ripley 2002), are very similar. The median R-magnitude of the GCs is $m_R = 21.75$. The brightest (faintest) cluster has a magnitude of $m_R = 18.8$ (22.97).

Can our spectroscopic dataset, which contains 656 GCs with known colours, be regarded as a photometrically representative subsample of the NGC 1399 GCS? As mentioned in Sect. 2.1, the colours and magnitudes of our GC sample are taken from the D+03 photometric study. These authors found a bimodal colour distribution for GCs in the magnitude range $21 < m_R < 23$. The brightest GCs, however, were discovered to have a unimodal distribution, peaking at an intermediate colour of $C - R \simeq 1.55$.

Figure 7 (upper right panel) shows the colour distribution of our sample. The main features described by D+03 are also found for the spectroscopic data set: the distribution is clearly bimodal, and the blue GCs show a peak near $C-R \simeq 1.3$. Following D+03 (and Paper I), we adopt $C-R = 1.55$ as the colour dividing blue from red GCs.

Further, the brightest clusters ($m_R < 21.1$, grey histogram) do not seem to follow a bimodal distribution.

Given that the brightest GCs show no signs of colour bimodality, the division of these GCs into "blue" and "red" is be somewhat arbitrary/artificial. As will be shown in Sect. 5.4, the brightest GCs form indeed a kinematically distinct subgroup.

4.2. Spatial distribution

The lower left panel of Fig. 7 shows the radial distribution of the GCs with velocity measurements. Within the central 5′ there are more red than blue GCs, which is a consequence of the steeper number-density profile of the former (see Sect. 9.2). At large radii, there are slightly more blue than red GCs. The median (projected) distance from NGC 1399 is 5.′9, 6.′5, and 5.′4 for all, the blue and the red GCs, respectively. The galactocentric distances of the GCs lie in the range $1.'1 \le R \le 18.'3$, i.e. $6 \lesssim R \lesssim 100\,\mathrm{kpc}$. For comparison, the data set analysed in Paper I covered the range $1.'1 \le R \le 9.'2$. The lower sub-panel plots an estimate for the radial completeness of our spectroscopic sample: dots and squares show the number of GCs with velocity measurements divided by the number of GC candidates from the D+03 photometric catalogue for two different faint-end magnitude limits. Considering the brighter half of our GC sample (grey squares), the completeness lies above 50 per cent for radii between 2′ and 8′, and at about 14′, it drops below 25 per cent.

The bottom right panel in Fig. 7 shows the azimuthal distribution of the GCs (the position angle (PA) is measured North through East). The upper sub-panel plots radial distance versus PA, and the azimuthal completeness decreases drastically beyond ∼8′. The lower sub-panel shows the histogram of the azimuthal distribution. The paucity of GCs around −90°, 0°, 90° and 180° results from the choice of mask positions on the plane of the sky (cf. Fig. 1).

5. Sample definition and interloper removal

5.1. GC subpopulations

The principal division is the distinction between red and blue GCs, which, as shown in Paper I and D+03, respectively, behave differently with regard to kinematics and spatial distribution. However, one also has to consider that the brightest GCs seem to have a unimodal colour distribution (cf. Sect. 4.1, D+03). To see how the kinematic properties of the GC populations change

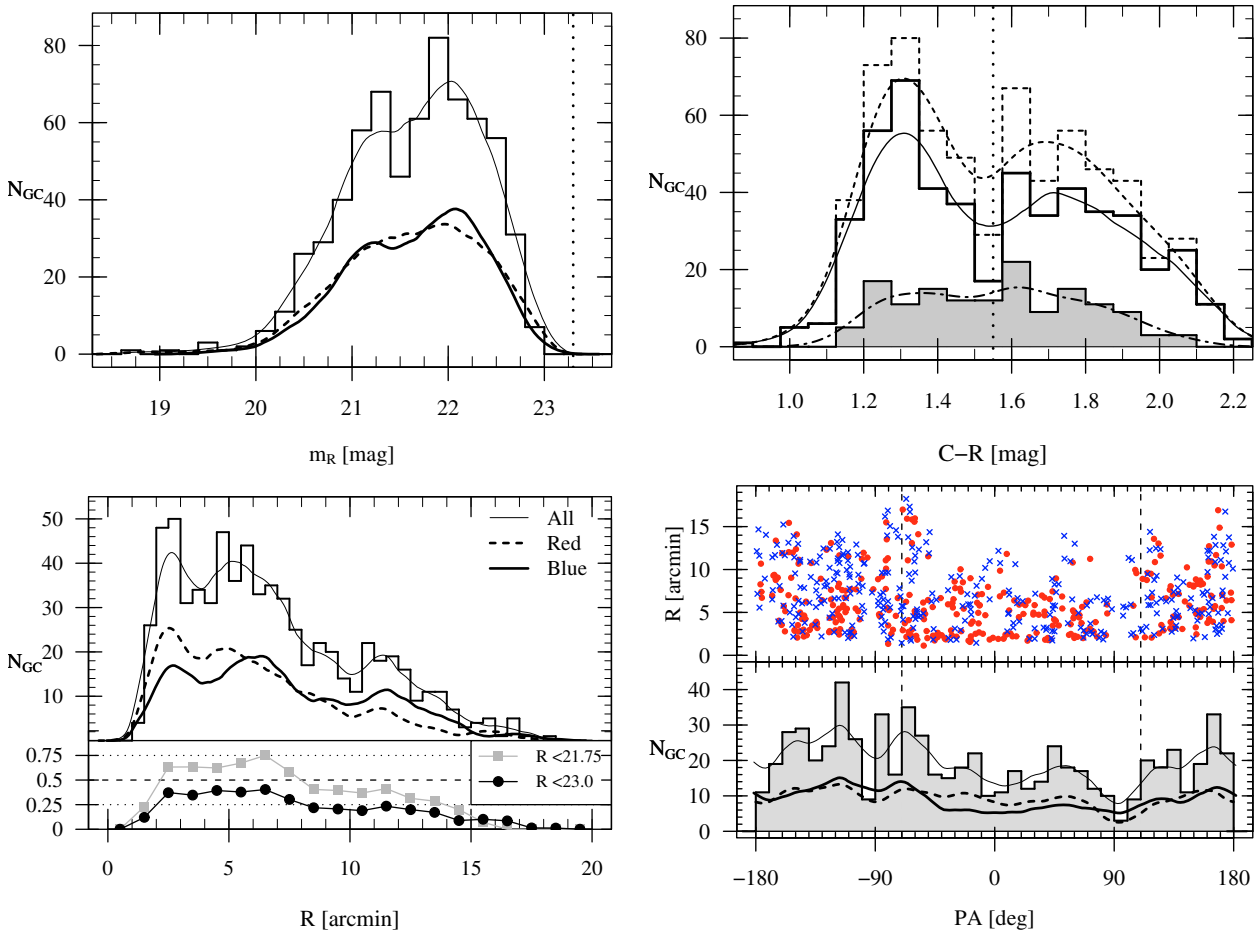

Fig. 7. NGC 1399 spectroscopic GC sample: photometric properties and spatial distribution. *Upper left*: GC luminosity distribution (bin width =0.2 mag). The dotted line at $m_R = 23.3$ indicates the turn-over magnitude of the GCS. The thin solid, thick solid and dashed lines show the kernel density estimates for all, the blue, and the red GCs, respectively. *Upper right panel*: colour distribution. The dashed histogram shows the distribution of all 656 velocity-confirmed GCs for which MOSAIC photometry is available, and the solid (unfilled) histogram are the GCs fainter than $m_R = 21.1$, and the grey histogram shows the distribution of the 144 brightest ($m_R < 21.1$) GCs. The dashed, solid and dot-dashed curves shows the respective kernel density estimate for the same data; a bandwidth of 0.075 mag was used (same as histogram bins). The dotted line at $C - R = 1.55$ indicates the limit dividing blue from red GCs. *Lower left*: radial distribution. The histogram (*upper sub-panel*) shows all 693 GCs with velocity measurements. The thin solid, thick solid and dashed lines show the kernel density estimates for all, the blue and the red GCs, respectively. The radial completeness, i.e. the number of GCs with velocity measurements with respect to the number of GC candidates ($0.9 < C - R < 2.2$) from the D+03 photometry is shown in the *lower sub-panel*. The black dots (grey squares) show the values for a faint-end magnitude limit of 23.0 (22.75). *Lower right*: azimuthal distribution of the GCs. The position angle (PA) is measured North over East, and the dashed vertical lines indicate the photometric major axis of NGC 1399 (110°). The *upper sub-panel* shows the radial distance from NGC 1399 vs. PA. Crosses and dots represent blue and red GCs, respectively. The histogram (*lower sub-panel*) has a bin width of 10°. The thin solid, thick solid and dashed lines show the kernel density estimates for all, the blue and the red GCs, respectively.

with the luminosity we plot in Fig. 8 the velocity dispersion as a function of R-magnitude. We divide the spectroscopic GC sample into blue and red GCs and calculate the line-of-sight velocity dispersion as a function of R-magnitude using a Gaussian window function (note that GCs brighter than $m_R = 20.0$ are omitted because of their sparse spacing along the x-axis). For all three kernels ($\sigma_{\rm mag} = 0.15, 0.2, 0.3$), the results are similar: for GCs with $20 \lesssim m_R \lesssim 21$, the dispersions of "blue" and "red" GCs are indistinguishable. For fainter GCs, down to about $m_R \simeq 22$, the blue and red GCs become well separated, and the respective dispersions do not appear to depend on the magnitude. For GCs fainter than $m_R \simeq 22$, however, the dispersions increase towards fainter magnitudes – probably a result of the larger velocity uncertainties (see Sect. 3.2). The quality selection (i.e. the inclusion of Class B measurements, shown as dashed curves in Fig. 8), does not have any impact on the detected features.

Guided by Fig. 8, we define the following samples for the dynamical analysis:

- B(lue) and $m_R \geq 21.1$ and $C-R \leq 1.55$ (256 GCs);
- R(ed) and $m_R \geq 21.1$ and $C-R > 1.55$ (256 GCs);
- F(aint) and $m_R \geq 21.1$ (512 GCs);
- BR(right) and $m_R < 21.1$ (144 GCs);
- The full sample contains A(ll) 693 GCs with radial velocity measurements.

The main quantity we extract from our dataset is the line-of-sight velocity dispersion $\sigma_{\rm los}$. Since dispersion measurements react very severely to the presence of outliers and sampling characteristics, it is important to remove possible contaminants.

As can already be seen from Fig. 1, our sample probably contains a number of GCs belonging to NGC 1404 ($v_{\rm helio} = 1947\,{\rm km\,s^{-1}}$). Our approach to identify these objects is detailed in Sect. 5.2.

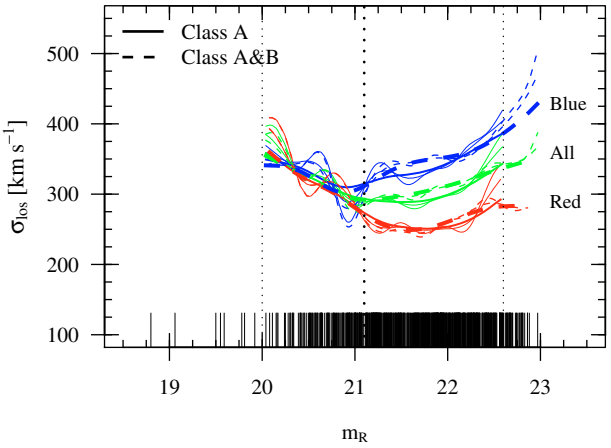

Fig. 8. Velocity dispersion as function of R-magnitude. For all GCs with $m_R > 20$, the dispersion is calculated using Gaussian kernels with a width of $\sigma_{mag} \in \{0.15, 0.2, 0.3\}$ mag. Dashed and solid curves show the values for the full and the "Class A" samples, respectively. The thick lines are the curves for $\sigma_{mag} = 0.3$. The dotted line at 22.6 mag indicates the magnitude limit for Class A spectra. The dashed line at 21.1 mag shows the division we adopt between bright and faint GCs. The ticks at the bottom of the panel show the R-magnitudes of the GCs.

Secondly, the presence of GCs with high relative velocities at large galactocentric radii (see Fig. 9, left panel) potentially has a large impact on the derived mass profiles. The treatment of these GCs with extreme velocities is discussed in Sect. 5.3.

In Sect. 5.4, we label the subsamples obtained from the samples defined above after the interloper removal.

5.2. NGC 1404 GC interloper removal

In the sky, NGC 1404 is the closest (giant) neighbour of NGC 1399. It lies 9′.8 southeast of NGC 1399, which corresponds to a projected distance of only 54 kpc. Its systemic velocity is 1947 km s^{-1} (NED[6]), which is inside the velocity range of GCs belonging to NGC 1399. Although NGC 1404 is reported to have an unusually low specific frequency of only $S_N \simeq 2$ (Richtler et al. 1992; Forbes et al. 1998), it is probable that GCs found in its vicinity belong to NGC 1404 rather than to NGC 1399. These GCs contaminate the NGC 1399 sample and would – if unaccounted for – lead us to overestimate the line-of-sight velocity dispersion and influence the measurement of the higher moments of the velocity distribution.

In Fig. 10 (left panel) we show the radial velocities of the GCs versus the projected distance from NGC 1404. Within 3′ from NGC 1404, the velocity distribution is skewed towards higher velocities, with two thirds of the GCs having velocities within 220 km s^{-1} of the NGC 1404 systemic velocity. The mean and median velocity of all GCs in this area are 1785 and 1936 km s^{-1}, respectively (the corresponding values are indicated by the dashed and solid arrows). Beyond 3′ from NGC 1404, the velocity field is clearly dominated by NGC 1399 GCs, and for the GCs within 3′–5′ of NGC 1404, we find a mean (median) velocity of 1510 (1475) km s^{-1}. Guided by these findings, we exclude all 23 (13 red and 10 blue) GCs within 3′ (≃16.6 kpc) of NGC 1404 from our analysis of the NGC 1399 GCS.

[6] NASA/IPAC Extragalactic Database
http://nedwww.ipac.caltech.edu

To distinguish the resulting sub-samples, we use Roman numerals as labels, assigning "I" to the unaltered samples listed in Sect. 5.1, and "II" to the data excluding the GCs in the vicinity of NGC 1404.

Beyond the scope of this paper remains the question whether the velocity structure in the vicinity of NGC 1404 is a superposition in the plane of the sky, or if it traces a genuine interaction between the galaxies and their GCSs (as modelled by Bekki et al. 2003). A more complete spatial coverage of the NGC 1404 region as well as a larger number of GC velocities in this area are required to uncover the presence of possible tidal structures.

5.3. Velocity diagrams and extreme velocities

Having dealt with the identification of GCs likely to belong to the neighbouring galaxy, we now study the velocity diagrams for the blue and red GC subpopulations. The main difference between red and blue GCs shown in Fig. 9 is that the red GCs are more concentrated towards the systemic velocity of NGC 1399, while the blue GCs have a larger range of velocities, implying a higher velocity dispersion for the latter. The red GCs occupy a wedge-shaped region in the diagram, suggesting a declining velocity dispersion.

We further find in both sub-panels GCs with large relative velocities which appear to deviate from the overall velocity distribution. The derived mass profile hinges on the treatment of these objects. As can be seen from Table 5 in Schuberth et al. (2006), the inclusion of only two interlopers at large radii is enough to significantly alter the parameters of the inferred dark matter halo.

The right panel of Fig. 9 shows the densities of the data points for the samples which will be used in the dynamical analysis. One notes that the (low-level) contours for the blue GCs are more irregular than those of the red GCs. Also, for radii between 20 and 40 kpc, the blue GCs seem to avoid the systemic velocity of NGC 1399. The velocity structure found for the blue GCs appears to be much more complex than that of red GCs.

The very concept of interlopers is inherently problematic: if we regard interlopers as an *unbound population*, we are able to identify only the extreme velocities and leave many undetected. Here we are primarily interested in a practical solution. To locate possible interlopers, we therefore chose an approach similar to the one described by Perea et al. (1990), who studied the effect of unbound particles on the results returned by different mass estimators (namely the virial mass estimator and the projected mass estimator as defined in Heisler et al. 1985). Perea et al. used a statistical "Jacknife" technique to identify interlopers in their N-body simulations of galaxy clusters. Since the spatial distributions of the GC subpopulations around NGC 1399 do not follow the mass distribution (which is at variance with the underlying assumption of the virial mass estimator), we choose the *tracer mass estimator* (TME, Evans et al. 2003) which can be generalised to the case where the number density of the tracer population is different from the overall mass density.

The method we use works as follows: for a set of N GCs, we first calculate the quantity m_N:

$$m_N = \langle v^2 \cdot R \rangle = C_{\rm proj} \cdot M_{\rm TME}, \quad (1)$$

which is proportional to $M_{\rm TME}$, the tracer mass estimate, and where v is the line-of-sight velocity relative to the NGC 1399 systemic velocity and R is the projected distance from NGC 1399. We then select, as potential outlier, the GC

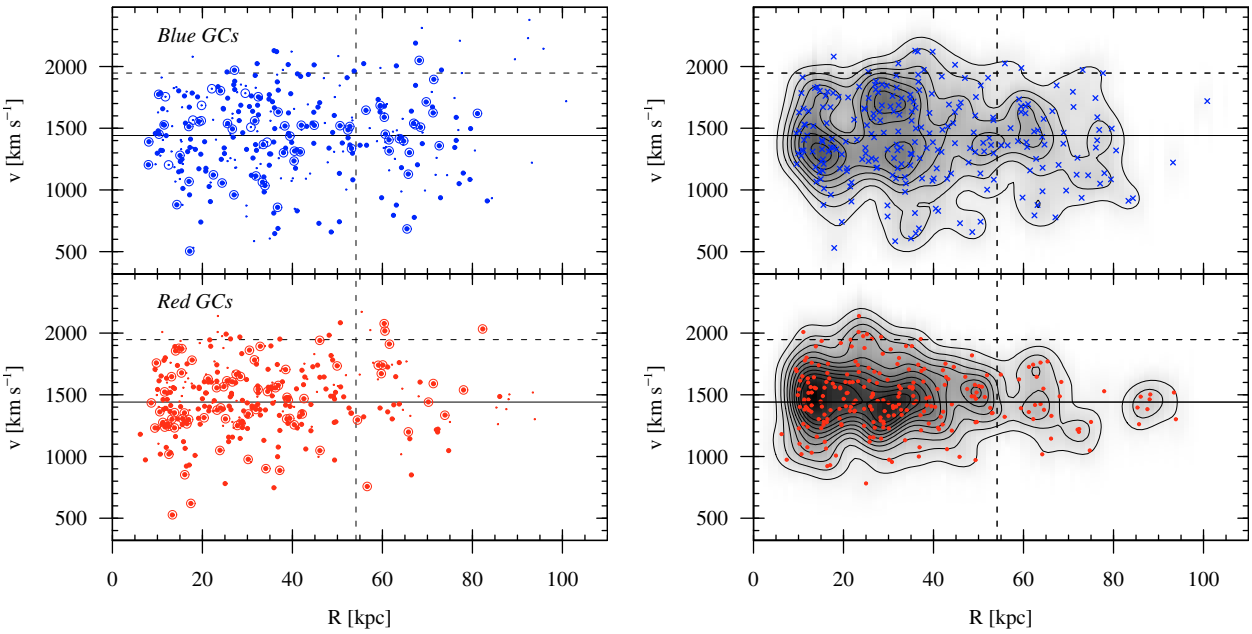

Fig. 9. NGC 1399 GC velocities. *Left panel*: velocities vs. galactocentric distance for the blue and red GC sample (shown in the upper and lower sub-panel, respectively). Large and small dots show GCs with "Class A" and "B" velocity measurements, respectively. Objects brighter than $m_R = 21.1$ are marked by circles. The dashed line at 54 kpc shows the projected distance of NGC 1404. The solid and dashed horizontal lines indicate the systemic velocities of NGC 1399 and NGC 1404, respectively. *Right*: densities for the data points for the blue and red samples (BIII and RIII cf. 5.4) shown as grey-scale and contour plot. The blue subsample appears to exhibit substructure which is not present in the red.

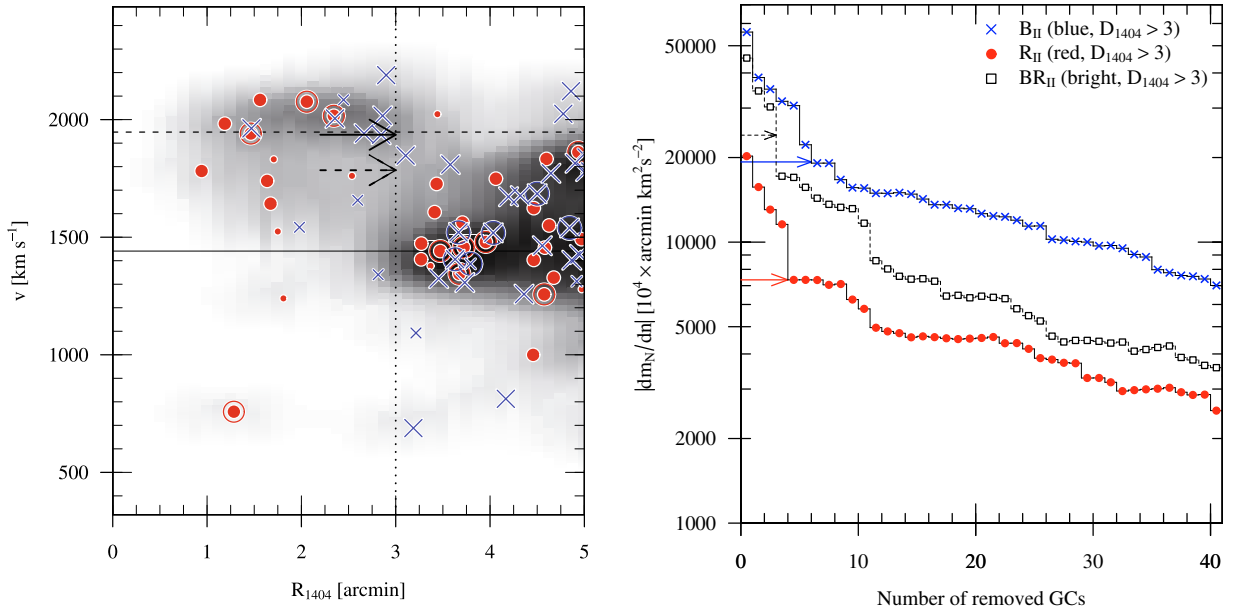

Fig. 10. Interloper removal. *Left*: velocities vs. distance from NGC 1404. Crosses and dots represent blue and red GCs, respectively. Large and small symbols refer to Class A and B velocity measurements, respectively. Bright GCs ($m_R < 21.1$ mag) are marked by a circle. The systemic velocities of NGC 1399 and NGC 1404 are shown as solid and dashed lines, respectively. The dotted line at 3′ is the limit we adopt to separate NGC 1404 GCs from the ones belonging to NGC 1399. The dashed and solid arrow indicate the mean and median velocity of the GCs within 3′, respectively. The grey-scale shows the density of the data points smoothed with a Gaussian ($\sigma_x = 0.'5$, $\sigma_y = 75$ km s^{-1}). *Right*: interloper removal using the tracer mass estimator (TME). The magnitude of the derivative of m_N (cf. Eq. (1)) as function of n, the number of eliminated interloper candidates. Crosses and dots show red and blue GCs ($m_R > 21.1$, $D_{1404} > 3'$), respectively. The bright GCs are shown as rectangles. The arrows indicate the number of rejected GCs for the different samples (BII: 6, RII: 4, and BRII: 3 GCs).

which has the largest contribution i.e. max($v^2 \cdot R$), remove it from the list and calculate

$$m_i = \frac{1}{(N-1)} \sum_{j \neq i}^{N} {v_j}^2 \cdot R_j, \qquad (2)$$

the expression for the remaining $(N - 1)$ GCs. This procedure is repeated and, in the right panel of Fig. 10, we plot the magnitude of the derivative of m_N with respect to n, the number of eliminated GCs.

Obviously, selectively culling the high relative velocities at large distances drastically lowers the estimate for the total mass,

resulting in large values of $|dm_N/dn|$. Once the algorithm with increasing n starts removing objects from the overall velocity field, the mass difference between steps becomes smaller.

As can be seen from the right panel of Fig. 10, a convergence is reached after removing four GCs from the red subsample RII. For the blue GCs (BII), the situation is not as clear, and we decide to remove six GCs. For the bright GCs, we remove three GCs.

As opposed to the constant velocity cuts (at v_{helio} = 800 and 2080 km s^{-1}) used in Paper I, this algorithm does not introduce a de facto upper limit on line-of-sight velocity dispersion.

Compared to schemes which use a jackknife to search for 3σ deviations in a local (∼15 neighbours) velocity field (which may be ill-defined in the sparsely sampled outer regions), our approach also works when the rejected GC is not the only deviant data point in its neighbourhood.

5.4. Defining the subsamples

To assess the impact of the interloper removal discussed in the preceding sections, we assign the following labels: the primary label indicates the parent sample (All, BRight, Faint, Blue, and Red, cf. Sect. 5.1), and the Roman numerals I–IV refer to the *sequence* of interloper removal applied:

I: full data set, no interloper removal;
II: GCs within 3′ of NGC 1404 removed (Sect. 5.2);
III: extreme velocities removed via TME algorithm (Sect. 5.3);
IV: restriction to Class A velocity measurements.

To expand the radial coverage, we define the "extended" samples AV, BV, and RV where we include the GC velocities presented by B+07 (with the Washington photometry given in Schuberth et al. 2008). From the list of B+07, we use all Class A GCs classified as intra-cluster GCs (ICGCs), plus the GCs in the vicinity of NGC 1399 while excluding GCs within 3′ of NGC 1404. These GCs are shown as large triangles in the upper panels of Fig. 13 where we plot the GC velocities versus the distance from NGC 1399. Since most GCs in the list of B+07 are brighter than m_R = 21.1, no bright-end magnitude cutoff is applied to the "extended" samples.

The basic statistical properties of the samples defined above are listed in Table 3 and discussed in the following section.

6. The line-of-sight velocity distribution

We expect the line-of-sight velocity distribution (LOSVD) to be nearly Gaussian. Deviations from Gaussianity may be caused by orbital anisotropies, the presence of interlopers, strong variations of the velocity dispersion profiles with radius, or rotation. Our sample, being the largest of its kind so far, allows us to test the statistical properties of the LOSVD in detail.

Table 3 summarises the statistical properties of the velocity samples defined in Sect. 5.4. Besides the first four moments of the distributions (i.e. mean, dispersion, skewness, and kurtosis), we list the p-values returned by the Anderson-Darling (AD) and Kolmogorov-Smirnov (KS), and the Shapiro-Wilks (SW) tests for normality. With the exception of the dispersion which we calculate using the expressions given in Pryor & Meylan (1993), the data listed in Table 3 were obtained using the functions of the `e1071` and `nortest` packages in R-statistics software[7] for the higher moments and the normality tests, respectively.

[7] R Development Core Team (Ihaka & Gentleman 1996) http://www.r-project.org.

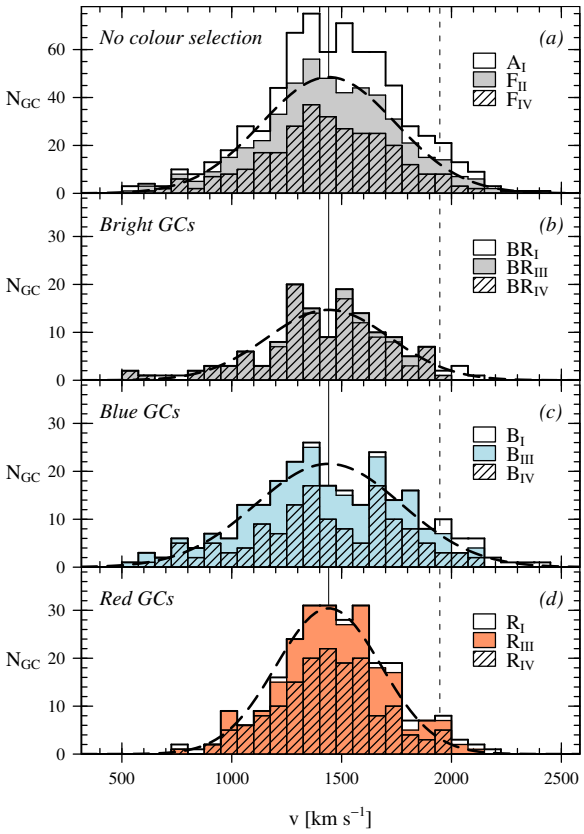

Fig. 11. Velocity histograms. **a)**: the unfilled histogram shows all 693 GCs (AI). The solid histogram bars are the faint (m_R > 21.1) GCs outside the 3′ radius around NGC 1404 (i.e. sample FII), and the dashed histogram is the same for the "Class A" velocity measurements after outlier rejection (sample FIV). **b)**: the bright (m_R ≤ 21.1) GCs, BRI, BRIII, and BRIV. Panels **c)** and **d)** show the same for blue and red GCs, respectively. In all panels, the solid and dashed vertical lines show the systemic velocity of NGC 1399 and NGC 1404, respectively. The dashed curve is a Gaussian with the width as given in Table 3 for the data represented as solid histogram (i.e. FII, BRIII, BIII, and RIII, respectively). Note that the range of the y-axis has been adjusted for easier comparison, with panel **a)** having twice the range of the subsequent plots.

The SW test (Shapiro & Wilk 1965; Royston 1982) is one of the most popular tests for normality which also works for small samples. The Anderson-Darling (Stephens 1974) test is a variant of the KS-test tailored to be more sensitive in the wings of the distribution. The SW and AD tests are among the tests recommended by D'Agostino & Stephens (1986); note that these authors caution against the use of the KS test which has a much smaller statistical power. A detailed discussion of the application of the AD test in the context of galaxy group dynamics is given in Hou et al. (2009). These authors compare the performance of the AD test to the more commonly used KS and χ^2 tests and find that the AD test is the most powerful of the three. They conclude that it is a suitable statistical tool to detect departures from normality, which allows the identification of dynamically complex systems.

The velocity histograms for the entire, the "bright", the red and the blue sample are shown in Fig. 11. In all four sub-panels, we plot the corresponding samples prior to any interloper removal (unfilled histograms). The solid histogram bars show the data after removing GCs in the vicinity of NGC 1404 and the GCs identified by the M_{TME}-algorithm (in panel *a*, the solid

histogram also excludes the bright GCs). The dashed bars show these samples when restricted to "Class A" velocity measurements. The striking difference between the velocity distributions of red and blue GCs is that the red GCs seem to be well represented by a Gaussian while the blue GCs appear to avoid the systemic velocity. Also the distribution of the bright GCs seems to be double-peaked.

Below we examine whether these distributions are consistent with being Gaussian.

6.1. Tests for normality

Adopting $p \leq 0.05$ as criterion for rejecting the Null hypothesis of normality, we find that *none of the bright* subsamples (BRI–BRIV) is consistent with being drawn from a normal distribution.

The fact that the full sample (AI, AII, AV) deviates from Gaussianity (at the ~90 per level) appears to be due to the presence of the bright GCs: the velocity distribution of objects fainter than $m_R = 21.1$ mag (sample FII is the union of BII and RII) cannot be distinguished from a Gaussian.

For the red subsamples (RI through RIV), a Gaussian seems to be a valid description. Only the "extended" sample (RV) performs worse (probably because it encompasses bright GCs), where the hypothesis of normality is rejected at the 91% level by the KS-test.

While the full blue data set and the sample after removing the GCs near NGC 1404 (BI and BII) are consistent with being Gaussian, the outlier rejection (BIII) and restriction to the "Class A" velocities (BIV) lead to significantly lower p-values. In the case of the latter, all tests rule out a normal distribution at the 90% level, which appears reasonable given that the distribution has a pronounced dip (cf. Fig. 11, panel *(c)*, dashed histogram).

Below we address in more detail the deviations from Gaussianity, as quantified by the higher moments of the LOSVD.

6.2. Moments of the LOSVD

6.2.1. Mean

Assuming that the GCs are bound to NGC 1399, the first moment of the LOSVD is expected to coincide with the systemic velocity of the galaxy, which is $1441 \pm 9\,\mathrm{km\,s^{-1}}$ (Paper I). As can be seen from the third column in Table 3, this is, within the uncertainties, the case for all subsamples, with the exception of RI, where the GCs in the vicinity of NGC 1404 are responsible for increasing the mean velocity.

6.2.2. Dispersion

The second moments (Table 3, Col. 5), the dispersions, are calculated using the maximum-likelihood method presented by Pryor & Meylan (1993), where the individual velocities are weighted by their respective uncertainties. Note that these estimates do not differ from the standard deviations given in Col. 4 by more than $5\,\mathrm{km\,s^{-1}}$. The interloper removal, by construction, lowers the velocity dispersion. The largest decrease can be found for the blue GCs, where the difference between BI and BIII is $25\,\mathrm{km\,s^{-1}}$. For the red sample, the corresponding value is $17\,\mathrm{km\,s^{-1}}$. We only consider at this stage the full radial range of the sample. As will be shown later, the effect of the interloper removal on the dispersion calculated for individual radial bins can be much larger.

The main feature is that the dispersions for the blue and red GCs differ significantly, with values of 333 ± 16 and $239 \pm 11\,\mathrm{km\,s^{-1}}$ for the blue and red samples (BIII and RIII), respectively. The corresponding values given in Paper I (Table 2) are $\sigma_{\mathrm{blue}} = 291 \pm 14$ and $\sigma_{\mathrm{red}} = 255 \pm 13$. The agreement for the red GCs is good, and the discrepancy found for the blue GCs is due to the different ways of treating extreme velocities: in Paper I such objects were culled from the sample by imposing radially constant velocity cuts (at 800 and $2080\,\mathrm{km\,s^{-1}}$), while the method employed here (see Sect. 5.3) does not operate with fixed upper/lower limits, which leads to a larger dispersion.

6.2.3. Skewness

Coming back to the issue of Gaussianity, we calculate the third moment of the LOSVD: the skewness is a measure of the symmetry of a distribution (the Gaussian, being symmetric with respect to the mean, has a skewness of zero):

$$\mathrm{skew} = \frac{1}{N}\sum_{j=1}^{N}\left[\frac{x_j - \bar{x}}{\sigma}\right]^3 . \tag{3}$$

The uncertainties were estimated using a bootstrap (with 999 resamplings). We consistently find a *negative* skewness for the bright subsamples (BRI-BRIV, Fig. 11b), i.e. there are more data points in the low-velocity tail of the distribution.

The blue GCs also show a *negative* skewness, which is significant for the samples BIII and BIV (cf. Fig. 11c). A similar finding was already described in Paper I.

The distribution of the red GCs is symmetric with respect to the systemic velocity, as is to be expected for a Gaussian distribution (cf. Fig. 11d).

6.2.4. Kurtosis

In the following, κ denotes the *reduced kurtosis*, or *kurtosis excess* (to assign the value zero to a normal distribution), i.e.:

$$\kappa = \frac{1}{N}\sum_{j=1}^{N}\left[\frac{x_j - \bar{x}}{\sigma}\right]^4 - 3 . \tag{4}$$

The reduced kurtosis κ for the various subsamples of our data is given in Col. 7 of Table 3. The uncertainties $\Delta\kappa$ were again estimated using a bootstrap. The brightest GCs have (marginally significant) positive kurtosis values, meaning that the distribution is more "peaked" than a Gaussian.

The blue samples (BI–BIV), on the other hand, have a negative kurtosis, indicative of a more flat-topped distribution which might be the result of a tangential orbital bias.

The red GCs are consistent with $\kappa = 0$, which would be expected in the case of isotropic orbits.

6.3. Summary of the statistical tests

We briefly summarise the main findings from the above statistical considerations. The velocity dispersions of the red and blue subsamples are, as in Paper I, significantly different, with the blue GCs showing a larger dispersion. We note that the dispersions of the bright ($m_R < 21.1$) subsamples have values in between those found for the red and blue GCs.

The entirety of the GCs (AI, AII) is not Gaussian, which is most likely due to the pronounced skewness of the brightest GCs.

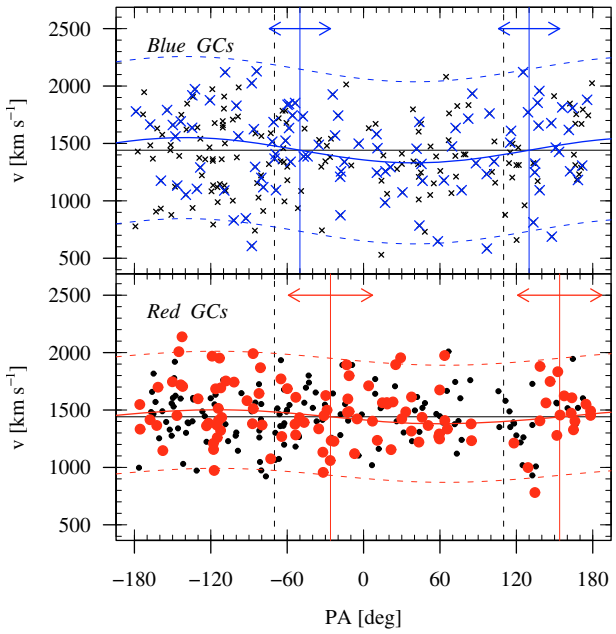

Fig. 12. Rotation of the NGC 1399 GCS. Velocities versus position angle. The *upper panel* shows the data for the blue sample BIII (i.e. the data after the removal of the GCs in the vicinity of NGC 1404 and the outlier rejection) for the azimuthally complete radial interval $R \leq 8\farcm0$. Large symbols are GCs in the "outer" ($4 < R \leq 8\farcm0$) region for which a significant rotation signal is found. The solid curve shows the best-fit sine-curve for this sample, the dashed curves indicate the $\pm 2 \cdot \sigma_{\rm los}$ boundaries, where $\sigma_{\rm los} = 353 \pm 26\,{\rm km\,s^{-1}}$. The vertical solid lines and arrows indicate Θ_0 and $\Delta\Theta_0$, respectively. The *lower panel* shows the same for the red GCs (sample RIII). The velocity dispersion of the red GCs in the "outer" interval is $\sigma_{\rm los} = 255 \pm 19\,{\rm km\,s^{-1}}$. In both panels, the vertical dashed lines indicate the position angle (photometric major axis) of NGC 1399 (110°). The respective fit parameters are listed in Table 4.

The blue subsamples, although formally consistent with being Gaussian, show (after the outlier rejection) significantly negative values for both skewness and kurtosis.

The red GCs are well represented by a Gaussian, which would be expected in the case of isotropic orbits.

7. Rotation

The amount of rotation found in a GCS and among its subpopulations might be indicative of the host galaxy merger history. The presence of rotation (rather than the absence thereof, since one only observes projected rotation), might help constrain GCS formation scenarios.

In Paper I, we did not find any signature of rotation, with the exception of the outer ($R > 6'$) metal-poor GCs, for which a marginal rotation amplitude of $68 \pm 60\,{\rm km\,s^{-1}}$ was detected (for a position angle of $\Theta_0 = 140° \pm 39°$). Our revised and extended data set provides the opportunity to re-examine this finding.

We apply the method used in Paper I, which consists of fitting a sine-curve to the velocities plotted versus the position angle (as shown in Fig. 12):

$$v_{\rm rot}(\Theta) = v_{\rm sys} + A_{\rm rot} \sin(\Theta - \Theta_0). \quad (5)$$

Further, to ensure that the rotation signal is not merely an artifact of the inhomogeneous spatial and azimuthal coverage, we calculate the rotation amplitude for 1000 Monte Carlo (MC) realizations, in which we keep the positions of our original dataset but permutate the velocities. From this we determine the fraction f of MC runs for which a rotation amplitude *larger* than the observed one was found: i.e. the smaller the value of f, the higher the significance of the rotation signal.

Table 4 lists the values for various GC subsamples. Since, as can be seen from Fig. 7 (bottom right panel), the azimuthal coverage becomes very patchy for galactocentric distances beyond about $8\farcm0$ (≃44 kpc), we also give the results for the radial range $0' \leq R \leq 8\farcm0$, where the spatial coverage is more uniform and the completeness (cf. Fig. 7, bottom left panel) is relatively high. This selection is then further divided into an "inner" ($0' \leq R \leq 4\farcm0$) and an "outer" ($4\farcm0 < R \leq 8\farcm0$) region.

7.1. Rotation of the brightest GCs

The brightest GCs ($m_R < 21.1$), show no sign of rotation. For all selections (BRI-BRIV) and radial intervals considered in Table 4, the rotation amplitude is consistent with being zero.

7.2. Rotation of the metal-rich GCs

For the metal-rich GCs, only the sample RIII (i.e. the data set obtained after masking the GCs in the vicinity of NGC 1404 and applying the outlier rejection algorithm) shows a weak rotation signal ($A = 61 \pm 35\,{\rm km\,s^{-1}}$, $\Theta = 154 \pm 33°$) for the "outer sample". The data and the fit are shown in the lower panel of Fig. 12. The corresponding f-value of 0.27 shows that a rotation signal of this magnitude arises from the randomised data with a probability of 27 per cent, meaning no significant rotation is detected for the red GCs. Moreover, this weak rotation signal vanishes completely when only the "Class A" velocity measurements are considered (RIV).

7.3. Rotation of the metal-poor GCs

Within the central $4\farcm0$ (≃22 kpc), none of the blue GC subsamples shows any rotation signal. For the "outer samples", however, the rotation amplitudes lie in the range $110-126\,{\rm km\,s^{-1}}$, and the values obtained for Θ_0 agree within the uncertainties. For the blue GCs BII (after removal of GCs near NGC 1404), the amplitude is $A = 110 \pm 53\,{\rm km\,s^{-1}}$, and $\Theta_0 = 130 \pm 24°$ (see Fig. 12, upper panel), which agrees with the rotation values quoted in Paper I. After further restricting this sample to "Class A" velocities, the results agree very well, although the smaller number of data points leads to larger uncertainties. We caution, however, that the probability of such an amplitude resulting from the randomised data still is about 10 per cent.

7.4. NGC 1399 and the rotation of its GCS

As stated above, we find no rotation for the red (metal-rich) GC population. In this respect, the red GCs appear to reflect the properties of the stellar body of NGC 1399 for which the spectroscopic study by Saglia et al. (2000) found only a small ($\lesssim 30\,{\rm km\,s^{-1}}$) rotation along the major axis (an equally small signal was found for the slightly off-centre slit position parallel to the minor axis).

For the blue GCs, a significant rotation signature is found for the radial range between 4 and 8 arcminutes. The axis of rotation is consistent with the photometric major axis of NGC 1399 (PA = 110°). Due to the very patchy angular coverage for radii beyond about 8′, no statement about the rotation of the GCs beyond ∼44 kpc can be made.

Table 4. Rotation amplitudes and angles for the different subsamples.

	$0' \le R \le R_{\rm max}$				$0' \le R \le 8'.0$				$0' \le R \le 4'.0$				$4' < R \le 8'.0$			
ID	$N_{\rm GC}$	Θ_0	$A_{\rm rot}$	f	$N_{\rm GC}$	Θ_0	$A_{\rm rot}$	f	$N_{\rm GC}$	Θ_0	$A_{\rm rot}$	f	$N_{\rm GC}$	Θ_0	$A_{\rm rot}$	f
(1)	(2)	(3)	(4)	(5)	(6)	(7)	(8)	(9)	(10)	(11)	(12)	(13)	(14)	(15)	(16)	(17)
AI	693	109 ± 19	48 ± 16	0.02	476	132 ± 27	40 ± 19	0.12	193	152 ± 123	14 ± 29	0.88	283	130 ± 24	59 ± 25	0.06
AII	670	134 ± 26	36 ± 16	0.10	472	143 ± 29	39 ± 19	0.17	193	152 ± 123	14 ± 29	0.84	279	142 ± 26	56 ± 25	0.12
FII	493	141 ± 27	42 ± 19	0.09	347	143 ± 27	47 ± 22	0.10	142	170 ± 110	17 ± 32	0.87	205	139 ± 24	71 ± 30	0.05
FIV	297	127 ± 48	27 ± 24	0.56	218	146 ± 31	46 ± 28	0.19	88	207 ± 128	18 ± 39	0.87	130	136 ± 26	73 ± 38	0.12
BRI	144	91 ± 57	36 ± 35	0.6	102	160 ± 170	14 ± 41	0.91	45	139 ± 473	8 ± 74	0.99	57	169 ± 150	20 ± 48	0.94
BRII	140	100 ± 85	24 ± 34	0.79	102	160 ± 170	14 ± 41	0.98	45	139 ± 473	8 ± 74	1	57	169 ± 150	20 ± 48	0.95
BRIII	137	109 ± 77	26 ± 32	0.71	102	160 ± 170	14 ± 41	0.94	45	139 ± 473	8 ± 74	1	57	169 ± 150	20 ± 48	0.95
BRIV	127	107 ± 114	18 ± 35	0.89	93	230 ± 173	14 ± 46	0.95	39	259 ± 124	36 ± 85	0.93	54	144 ± 327	9 ± 49	1
BI	256	113 ± 18	93 ± 32	0	161	118 ± 24	87 ± 39	0.12	59	136 ± 108	32 ± 55	0.91	102	118 ± 21	126 ± 53	0.039
BII	246	131 ± 24	75 ± 31	0.03	157	131 ± 28	76 ± 38	0.11	59	136 ± 108	32 ± 55	0.8	98	130 ± 24	110 ± 53	0.097
BIII	240	116 ± 29	59 ± 31	0.1	157	131 ± 28	76 ± 38	0.13	59	136 ± 108	32 ± 55	0.9	98	130 ± 24	110 ± 53	0.105
BIV	139	136 ± 54	41 ± 42	0.57	92	148 ± 32	79 ± 50	0.31	34	192 ± 117	33 ± 69	0.85	58	140 ± 26	123 ± 72	0.172
RI	256	108 ± 70	18 ± 22	0.66	190	164 ± 50	30 ± 26	0.46	83	222 ± 142	15 ± 39	0.9	107	154 ± 44	47 ± 36	0.46
RII	247	182 ± 89	14 ± 23	0.85	190	164 ± 50	30 ± 26	0.45	83	222 ± 142	15 ± 39	0.95	107	154 ± 44	47 ± 36	0.440
RIII	243	159 ± 61	20 ± 21	0.69	189	162 ± 40	37 ± 26	0.37	83	222 ± 142	15 ± 39	0.88	106	154 ± 33	61 ± 35	0.272
RIV	158	102 ± 94	16 ± 27	0.83	126	132 ± 76	22 ± 32	0.76	54	246 ± 275	11 ± 46	0.97	72	119 ± 56	41 ± 39	0.61

Notes. The first column lists the sample identifiers. Columns 2 through 4 give the number of GCs, the parameters obtained by fitting Eq. (5) to the data over the full radial range. Column 5 gives the fraction f of MC runs for which $A_{\rm MC} \ge A_{\rm rot}$ (see text for details). Columns 6–9, 10–13, and 14–17 give the GC numbers and parameters obtained when restricting the radial range to $0 \le R \le 8'.0$, $0 \le R \le 4'.0$, and $4 < R \le 8'.0$, respectively.

In the literature the amount of rotation is quantified in terms of the parameter $v_{\rm rot}/\sigma_{\rm los}$, (i.e. the ratio of rotational velocity to velocity dispersion). For NGC 1399 we find $v/\sigma \simeq 0$ for the metal-rich GCs and $v/\sigma \lesssim 0.3$ for the metal-poor GCs.

8. Radial velocity dispersion profiles

The line-of-sight velocity dispersion as a function of the projected radius is the quantity we aim to reproduce with the Jeans models described in Sect. 9. The histograms displayed in Fig. 11 and the data given in Table 3 show that the blue and red subpopulations have significantly different velocity distributions, as is already known from Paper I. We calculate the dispersion profiles separately for both subpopulations. First, we determine the dispersion values using the same annular bins for both subpopulations and divide our data into radial bins covering the full radial range (starting at 1.0, 3.5, 5.5, 7.5, 9.5, 12.5, 15.5, and 30.0 arcmin). The limits of the bins are shown as dotted lines in the upper and middle panels of Fig. 13.

The middle panels of Fig. 13 show the radial dispersion profiles for the red and blue GCs. Circles show the values obtained for the GCs fainter than $m_R = 21.1$, prior to any interloper removal (samples RI and BI for red and blue GCs, respectively). The corresponding profiles obtained after removing the GCs in the vicinity of NGC 1404 and the most extreme velocities (samples RIII and BIII) are shown as filled squares. For the extended samples RV and BV, shown as diamonds, the number of GCs in a bin is given in parenthesis. The dispersion profiles for the fixed radial bins for the samples RI through RV and BI-BV are given in Table A.1.

Next, to obtain data points with similar statistical uncertainties, we fix the number of GCs per bin (and thereby allow for a larger range in radial extent of the bins). In the bottom panels of Fig. 13, we use a moving window containing 35 GCs to plot the samples RIII and BIII together with the extended samples containing the B+07 measurements RV and BV. The corresponding values are listed in Table A.2.

8.1. Dispersion of the metal-rich subpopulation

For RIII and RV, shown in the middle left panel of Fig. 13, we find that the velocity dispersion declines for radii beyond ~30 kpc, while the values for the sample RI (prior to any interloper rejection) even show an increasing dispersion. The removal of the GCs in the vicinity of NGC 1404 mostly affects the 4th bin where the dispersion drops from 260 ± 35 to $216 \pm 30\,{\rm km\,s^{-1}}$. Removing the three potential outliers in the 5th bin by means of the TME-algorithm lowers the dispersion by about $90\,{\rm km\,s^{-1}}$.

The bottom left panel of Fig. 13 compares the moving-bin results for the samples RIII and RV. Both samples show again a smooth decline of the dispersion for larger radii. The marginally higher values found for the RV data which include the B+07 velocities is likely due to the inclusion of brighter ($m_R \le 21.1$ mag) clusters which have a higher velocity dispersion than the fainter red GCs. The 3rd bin for RIII has a surprisingly high dispersion of $305 \pm 44\,{\rm km\,s^{-1}}$ which is 50 (67) $\,{\rm km\,s^{-1}}$ higher than the value found in the previous (next) bin. This rise is caused by a number of GCs at high velocities (cf. Fig. 9), leading to a mean velocity which exceeds the systemic velocity of NGC 1399 by $\sim 120\,{\rm km\,s^{-1}}$. In the upper panel of Fig. 14, where we show the dispersion in a semi-logarithmic plot, the deviation of this data point becomes even more evident. In the modelling presented in Sect. 10 this data point (marked by an asterisk in Table A.2) is omitted.

8.2. Dispersion of the metal-poor subpopulation

For the blue GCs (shown in the right panels of Fig. 13) the situation is more complicated in so far as the dispersion profile is not as smooth. For the full sample BI as shown in the middle right panel of Fig. 13, the dispersion rises quite sharply by over $100\,{\rm km\,s^{-1}}$ for the range between ~10 and 35 kpc where it reaches almost $400\,{\rm km\,s^{-1}}$ before levelling out at $\sim 360, {\rm km\,s^{-1}}$. The effect of the interloper removal is strongest for the fifth bin where removing five GCs (four of which are in the vicinity of NGC 1404 and one GC is rejected by the TME algorithm, sample BIII) decreases the dispersion by more than $50\,{\rm km\,s^{-1}}$. For

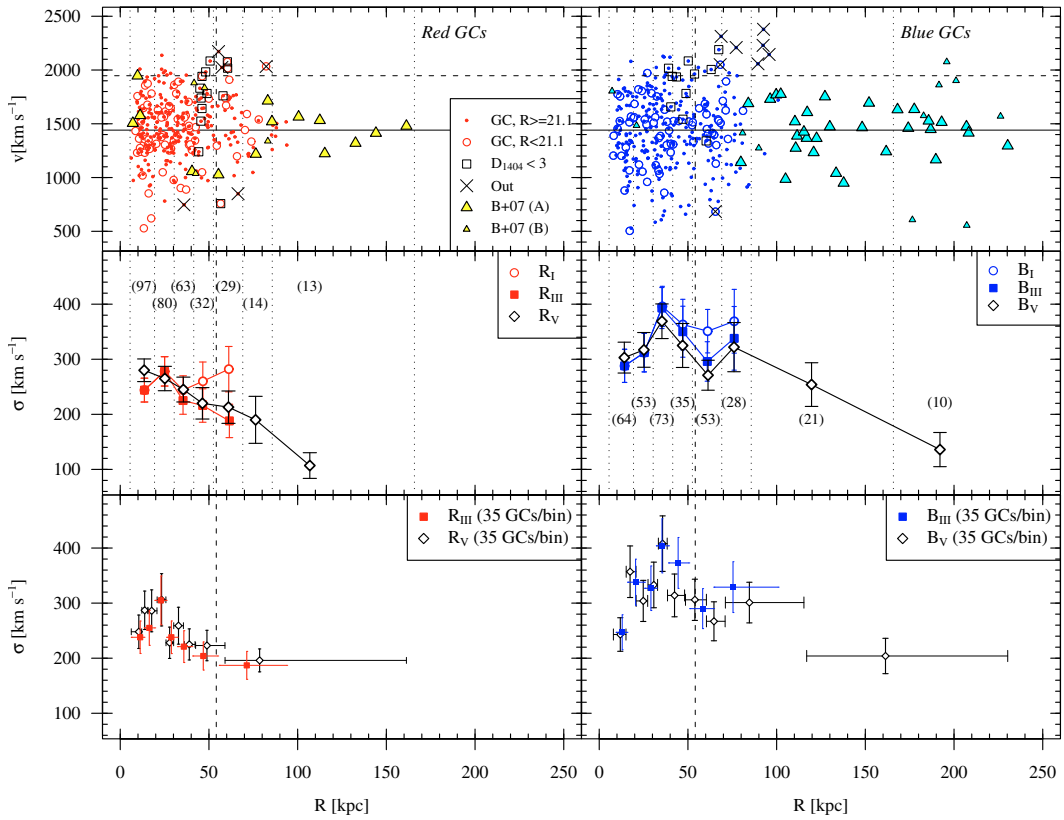

Fig. 13. Velocity diagrams and line-of-sight velocity dispersion profiles. *Upper left*: radial velocity vs. galactocentric distance for the red GCs. Dots and circles show faint and bright (m_R < 21.1 mag) GCs, respectively. Large and small triangles are the data points from Bergond et al. (2007) with Class A and B velocity measurements, respectively (see text for details). Squares mark GCs rejected on account of their proximity to NGC 1404; crosses are the GCs removed by the TME rejection algorithm. The solid and dashed horizontal lines are the systemic velocities of NGC 1399 and NGC 1404, respectively. The vertical dashed line shows the (projected) distance of NGC 1404. The dotted vertical lines show the radial bins for which the dispersion shown in the middle panels is calculated. *Upper right*: the same for the blue GCs. *Middle panels*: the dispersion profiles for fixed radial bins. Circles are the values obtained for the full samples (RI and BI) prior to any interloper removal. Filled squares show the values after removing GCs in the vicinity of NGC 1404 and the outliers identified by the TME algorithm (samples RIII and BIII). The dispersion profiles for the extended samples (RV and BV) including the velocities from Bergond et al. (2007) are shown as diamonds. The labels in parentheses give the number of GCs in a given bin. *Bottom panels*: filled squares are the profiles for RIII and BIII obtained for a moving bin comprising 35 GCs. Diamonds show the same for the samples RV and BV. These moving-bin profiles which are used for the modelling in Sect. 10 are listed in Table A.2.

the sixth bin, however, the dispersion is again somewhat higher (although the values agree within the uncertainties). For the sample BI and BIII no clear trend for the behaviour of the GCs towards larger radii is discernible.

Taking into account the velocities for the outer GCs by B+07 shows however, that also the blue GCs have a declining velocity dispersion profile (sample BV, shown as diamonds).

The lower right panel of Fig. 13 shows the velocity dispersion profiles for the samples BIII and BV for a moving window containing 35 GCs. Compared to the red GCs these profiles appear less continuous. This behaviour is likely due to inhomogeneities and substructures in the velocity field as illustrated in the right panel of Fig. 9.

8.3. Comparison to the stellar data

In Fig. 14 we compare our values to the results presented by Saglia et al. (2000). These authors used Gauss-Hermite polynomials to analyse absorption-line spectra of the stellar body of NGC 1399 out to 97″ (≃9 kpc). The radial ranges covered by both data sets only have a marginal overlap.

Stellar velocity dispersion profile: in the upper panel of Fig. 14 we plot the velocity dispersion profiles for the blue and red GCs (BIII, RIII) obtained for moving bins of 35 GCs (same as the bottom panels in Fig. 13). With the exception of the third data point, the red GCs appear to follow the trend shown by the stars in NGC 1399. Only the innermost blue data point is comparable to the stellar data, all subsequent bins show a much higher dispersion.

The fourth moment: in the lower panel of Fig. 14 we compare Gauss-Hermite h_4 values given by Saglia et al. to the corresponding values for the GCs which were converted from the κ values given in Table 3 using the following relation (van der Marel & Franx 1993):

$$\kappa \simeq 8\sqrt{6} \cdot h_4. \quad (6)$$

We find that the value for the blue GCs (sample BIII) lies significantly below the stellar values, while the value for the red GCs (RIII) seems to agree with the h_4 values of the stars. This figure also demonstrates that κ is not additive, which is illustrated by the grey area indicating the value obtained when combining the blue (BIII) and red (RIII) sample.

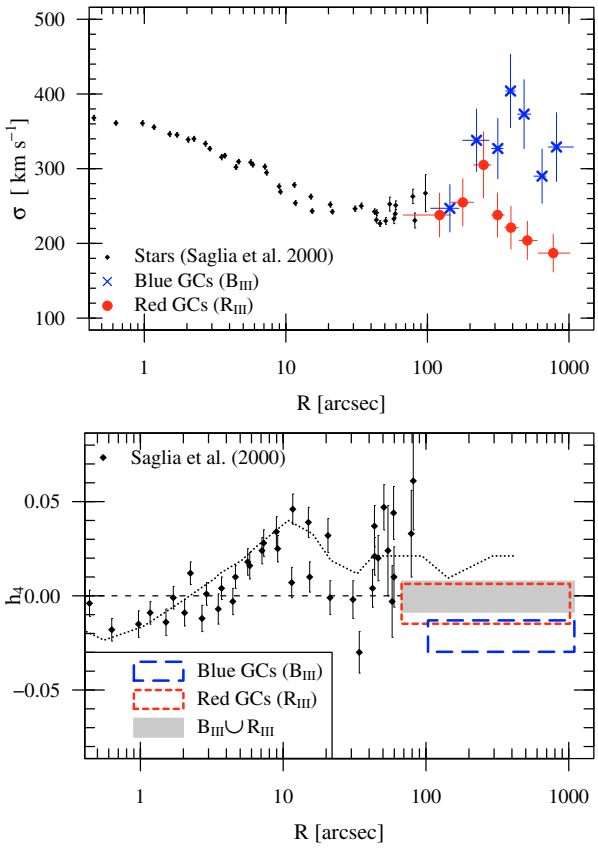

Fig. 14. Comparison to the stellar kinematics presented by Saglia et al. (2000). *Upper panel*: line-of-sight velocity dispersion profiles. Diamonds show the stellar kinematics, dots and crosses are our measurements of the red (RIII) and blue (BIII) GCs, respectively. *Lower panel*: Gauss-Hermite parameter h_4 (Eq. (6)) vs. projected radius. The values for the blue and red GCs are shown as long-dashed and dashed rectangle, respectively. The solid grey rectangle shows the value for the combined red and blue sample. The values derived from absorption-line spectroscopy by Saglia et al. (2000) are shown as diamonds, and the dashed line represents their best fit model (cf. their Fig. 5).

9. Jeans models

The mass profile of NGC 1399 is estimated by comparing the values derived from spherical, non-rotating Jeans models to the observed line-of-sight velocity dispersions. The assumption of spherical symmetry is justified by the near-spherical appearance of the galaxy. To account for the degeneracy between mass and orbital anisotropy, which can only be broken using much larger datasets than ours, we calculate models for different (constant) values of the anisotropy parameter β.

9.1. The Jeans equation

The spherical, non-rotating Jeans equation reads:

$$\frac{\mathrm{d}\left(\ell(r)\,\sigma_r^2(r)\right)}{\mathrm{d}r} + 2\,\frac{\beta(r)}{r}\,\ell(r)\,\sigma_r^2(r) = -\ell(r)\,\frac{G\cdot M(r)}{r^2}, \tag{7}$$

$$\text{with} \qquad \beta \equiv 1 - \frac{{\sigma_\theta}^2}{\sigma_r^2}.$$

Here, r is the true 3D radial distance from the centre and ℓ is the spatial (i.e., three-dimensional) density of the GCs; σ_r and σ_θ are the radial and azimuthal velocity dispersions, respectively.

Table 5. Globular cluster number density profiles.

	N_0 [GCs arcmin^{-2}]	R_0 [arcmin]	α	$\mathcal{B}\left(\frac{1}{2},\alpha\right)$
Red	28.43 ± 7.82	1.63 ± 0.34	1.02 ± 0.04	1.98
Blue	8.39 ± 1.05	2.91 ± 0.42	0.79 ± 0.03	2.32
All	35.54 ± 6.13	1.74 ± 0.27	0.84 ± 0.02	2.22

Notes. Fitting a cored power-law (Eq. (10)) to the data given in Table 2 of Bassino et al. (2006) yields the parameters listed above (the profile for "all" GCs was obtained by adding the number counts of the red and blue GCs).

β is the anisotropy parameter, $M(r)$ the enclosed mass and G is the constant of gravitation.

For our analysis, we use the expressions given by e.g. Mamon & Łokas (2005), see also van der Marel & Franx (1993). Given a mass distribution $M(r)$, a three-dimensional number density of a tracer population $\ell(r)$, and a *constant* anisotropy parameter β, the solution to the Jeans equation (Eq. (7)) reads:

$$\ell(r)\,\sigma_r^2(r) = \mathrm{G}\int_r^\infty \ell(s)\,M(s)\,\frac{1}{s^2}\left(\frac{s}{r}\right)^{2\beta}\mathrm{d}s. \tag{8}$$

This expression is then projected using the following integral:

$$\sigma_{\rm los}^2(R) = \frac{2}{N(R)}\left[\int_R^\infty \frac{\ell\sigma_r^2\,r\,\mathrm{d}r}{\sqrt{r^2-R^2}} - R^2\int_R^\infty \frac{\beta\ell\sigma_r^2\,\mathrm{d}r}{r\sqrt{r^2-R^2}}\right], \tag{9}$$

where $N(R)$ is the projected number density of the tracer population, and $\sigma_{\rm los}$ is the line-of-sight velocity dispersion, to be compared to our observed values. In the following, we discuss the quantities required to determine $\sigma_{\rm los}(R)$.

9.2. Globular cluster number density profiles

The GCS of NGC 1399 has been the target of two wide-field photometric studies. The work presented by (Bassino et al. 2006, hereafter B+06) extends the earlier D+03 study upon which the analysis presented in Paper I was based. For our analysis, we use a cored power-law profile (Reynolds-Hubble law) to fit the data from B+06:

$$N(R) = N_0\left(1+\left(\frac{R}{R_0}\right)^2\right)^{-\alpha}. \tag{10}$$

Here, R_0 is the core radius, and $2\cdot\alpha$ is the slope of the power-law in the outer region. For the above expression, the Abel inversion has an analytical solution (i.e. Eq. (10) can be deprojected exactly, e.g. Saha et al. 1996), and the three-dimensional number density profile reads:

$$\ell(r) = \frac{N_0}{R_0}\,\frac{1}{\mathcal{B}\left(\frac{1}{2},\alpha\right)}\cdot\left(1+\left(\frac{r}{R_0}\right)^2\right)^{-\left(\alpha+\frac{1}{2}\right)}, \tag{11}$$

where $\mathcal{B}$ is the Beta function. Table 5 lists the values obtained by fitting Eq. (10) to the number density profiles given in Table 2 of B+06. For the red GCs, the fit was performed for $R < 35'$, and $R < 45'$ for the blue/all GCs.

Figure 15 shows the number density profiles for the blue (open squares) and red GCs (circles) as given in B+06, together with the corresponding fits. One clearly sees that the red GCs have a steeper number density profile than the blue GCs. For

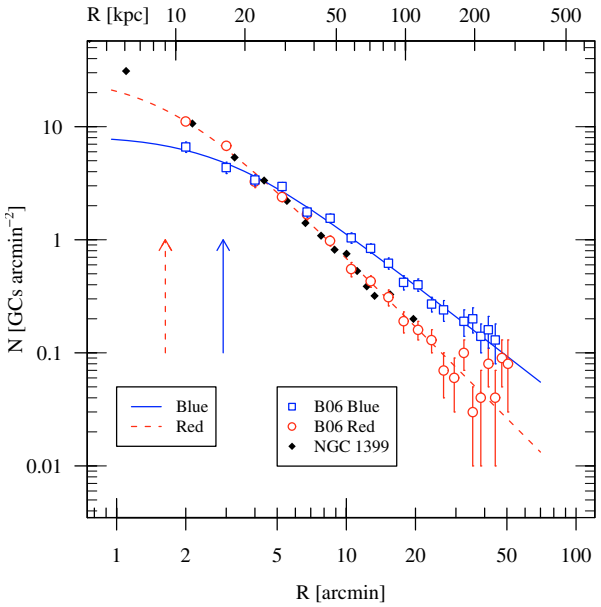

Fig. 15. GC number density profiles. The data from B+06 are shown together with the fits to Eq. (10). Circles and squares represent the red and blue GCs, respectively. The fits to the red and the blue number density distributions are shown as dashed and solid line, respectively. The coefficients are listed in Table 5. The dashed and solid arrows indicate the core radii R_0 as returned from the fits for the red and blue GCs, respectively. Diamonds show the surface brightness profile of NGC 1399, as given in Table 4 of D+03 (the data points have been shifted for comparison with the red GC number density profile).

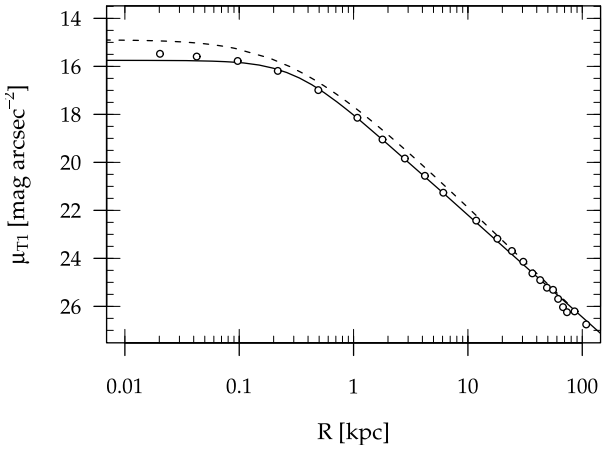

Fig. 16. Comparison between different deprojections of the surface brightness profile of NGC 1399: the dashed curve is the re-projection of the luminosity density profile as given in D+03 (Eq. (15)). The solid curve shows the fit to the data (Eq. (12)), which corresponds to the re-projection of Eq. (14).

reference, the surface brightness profile of NGC 1399 (as given by D+03, but scaled to match the red GC profile) is shown with diamonds. Note that in the region of overlap ($2' \lesssim R \lesssim 20'$) the slope of the densities of the stars and the red GCs are indistinguishable.

9.3. Luminous matter

In order to assess the dark matter content of NGC 1399, we first need a model for the luminous matter. Moreover, the spatial distribution of the stars is needed to model the stellar velocity dispersion profile (see Sect. 10.4.2).

9.3.1. Deprojection of the surface brightness profile

D+03 give the following fit to the R-band surface brightness profile of NGC 1399:

$$\mu(R) = 2.125 \log\left[1 + \left(\frac{R}{0\farcm055}\right)^2\right] + 15.75, \quad (12)$$

where R is the projected radius. Assuming an absolute solar luminosity of $M_{\odot,R} = 4.28$, the surface brightness profile in units of $L_\odot\,\mathrm{pc}^{-2}$ reads:

$$I(R) = 1.10 \times 10^4 \left[1 + \left(\frac{R}{0\farcm055}\right)^2\right]^{-0.85}. \quad (13)$$

At a distance of 19 Mpc, $0\farcm055$ correspond to 304 pc. Using Eq. (11) we obtain the deprojected profile (in units of $L_\odot\,\mathrm{pc}^{-3}$):

$$j(r)\left[\frac{L_\odot}{\mathrm{pc}^3}\right] = 16.33\left[1 + \left(\frac{r}{304\,\mathrm{pc}}\right)^2\right]^{-1.35}. \quad (14)$$

We now compare this to the deprojected profile given in D+03. These authors obtained the three-dimensional luminosity distribution by numerically projecting a cored power-law and compare the result to the fitted surface brightness profile. The luminosity density profile they obtained using this procedure reads:

$$L_{T_1}\left[\frac{L_\odot}{\mathrm{pc}^3}\right] = 101\left[1 + \frac{r}{221\,\mathrm{pc}}\right]^{-2.85}. \quad (15)$$

One notes that the central luminosity density of this profile is more than six times higher than what we find in Eq. (14). Further, the profile presented by D+03 is slightly steeper.

To show the difference between the two deprojections, we plot in Fig. 16 the surface brightness profile of NGC 1399 as given in Table 4 of D+03, together with the fit (Eq. (12), solid line) and the re-projection of their luminosity density profile (dashed line). The latter overestimates the measured surface brightness of NGC 1399 and therefore results in a larger stellar mass.

9.3.2. Stellar mass-to-light ratio

In Paper I, Richtler et al. quote an R-band stellar mass-to-light ratio of $M/L_R = 5.5$, which they obtained by converting the B-band value derived by Saglia et al. (2000). Recently, Gebhardt et al. (2007) used the Hubble Space Telescope to obtain kinematics for the very central part of NGC 1399 in order to measure the mass of the nuclear black hole. From their dynamical models, these authors find a best-fit $M/L_R = 5.2 \pm 0.4$ for a distance of 21.1 Mpc. At a distance of 19.0 Mpc, as assumed in this study, this corresponds to $M/L_R = 5.77 \pm 0.4$, which is in excellent agreement with the value given in Paper I. We thus adopt a stellar mass-to-light ratio of $\Upsilon_\star = M/L_R = 5.5$.

9.3.3. Enclosed stellar mass

We obtain the enclosed stellar mass by integrating Eq. (14):

$$M_{\mathrm{stars}}(R) = 4\pi\Upsilon_\star \int_0^R j(r) r^2 \mathrm{d}r, \quad (16)$$

which can be expressed in terms of the hypergeometric function:

$$M(R) = C_1 \cdot \frac{3}{4}\pi\Upsilon_\star R^3 \, {}_2F_1\left(\left[\frac{3}{2}, \gamma\right], \left[\frac{5}{2}\right], -\frac{R^2}{B^2}\right), \quad (17)$$

where $C_1 = 16.33$ is the constant, $B = 304$ pc the core radius, and $\gamma = 1.35$ is the exponent from Eq. (14). ${}_2F_1(a, b; c; z)$ is the hypergeometric function as defined in e.g. Abramowitz & Stegun (1964).

In practice, the hypergeometic function can be calculated to arbitrary precision (e.g. Press et al. 1992), but the computation of the integral over $M(R)$ becomes very time-consuming. In the programme calculating the Jeans-models, we therefore apply a piece-wise definition of the mass profile, using only standard functions: for radii smaller than 3430 pc, we use a 6th-order polynomial, and a 3rd-order polynomial in the range $3430 \le R \le 9200$. For $R > 9200$ pc the following expression is a good approximation to Eq. (17):

$$M(R) = C_2 \cdot 4\pi\Upsilon_\star R_{0,\star}^3 \times \left(\ln\left(1 + \frac{R}{R_{0,\star}} + \frac{R^2}{R_{0,\star}^2}\right) - \frac{R}{R_{0,\star}}\left(1 + \frac{R^2}{R_{0,\star}^2}\right)^{-1} + \sqrt{\frac{R}{R_{0,\star}}}\right), \quad (18)$$

where $R_{0,\star} = 1598$ pc, and $C_2 = 0.106$.

9.4. The anisotropy parameter β

The solutions to the Jeans equation given in Eq. (8) are defined for *constant* values of the anisotropy parameter. Since β cannot be determined from the data itself, we calculate our models for a set of anisotropy parameters. The higher moments derived in Sect. 8.3 suggest that the red cluster population is most likely isotropic, possibly slightly radial, while the blue GCs might show a mild tangential bias. We therefore use $\beta = -0.5, 0, +0.5$ for modelling the GCs.

9.5. Dark matter profiles

Numerical cosmological simulations predict cuspy dark matter density profiles (e.g. Bullock et al. 2001). However, the very inner shape apparently depends on numerical details (e.g. Diemand et al. 2005), while agreement is reached regarding the outer profile which declines as R^{-3}. Here we use an NFW (Navarro et al. 1997) halo to represent a cuspy dark component. The density profile is given by:

$$\varrho_{\rm NFW}(r) = \frac{\varrho_{\rm s}}{\left(\frac{r}{r_{\rm s}}\right)\left(1 + \frac{r}{r_{\rm s}}\right)^2}, \quad (19)$$

and the cumulative mass reads:

$$M_{\rm NFW}(r) = 4\pi\varrho_{\rm s} r_{\rm s}^3 \cdot \left(\ln\left(1 + \frac{r}{r_{\rm s}}\right) - \frac{\frac{r}{r_{\rm s}}}{1 + \frac{r}{r_{\rm s}}}\right). \quad (20)$$

However, in low surface brightness galaxies, where dark matter contributes significantly already in the central regions, most observations are not compatible with a cuspy halo (Gentile et al. 2007) but rather with a cored density profile. We therefore also model a dark matter density profile with a core. One possibility is to use the density profile, which Burkert (1995) introduced to represent the dark matter halo of dwarf galaxies. For this halo, the density profile is:

$$\varrho(r) = \frac{\varrho_0}{\left(1 + \frac{r}{r_0}\right)\left(1 + \frac{r^2}{r_0^2}\right)}, \quad (21)$$

and the cumulative mass is given by the following expression:

$$M(r) = 4\pi\varrho_0 r_0^3\left(\frac{1}{2}\ln\left(1 + \frac{r}{r_0}\right) + \frac{1}{4}\ln\left(1 + \frac{r^2}{r_0^2}\right) - \frac{1}{2}\arctan\left(\frac{r}{r_0}\right)\right). \quad (22)$$

10. Mass models for NGC 1399

In this section, we present the results of the Jeans modelling. First, we treat the tracer populations separately, i.e. we fit the velocity dispersion profiles of the red and blue GC samples using NFW halos. In a second step, we search for a set of parameters to describe both populations. The stellar velocity dispersion profile by Saglia et al. (2000) is then used to put further constraints on the mass model of NGC 1399. Finally, the results for the NFW halos are compared to cored Burkert halo models.

10.1. Jeans analysis

To obtain an estimate for the NGC 1399 mass profile, we compare the observed velocity dispersion profiles to Jeans models (Eq. (9)). The stellar mass-to-light ratio is assumed to be constant (see Sect. 9.3), and the (constant) anisotropy parameter takes the values $\beta = -0.5, 0$, or $+0.5$ (corresponding to a mild tangential, isotropic, and a slightly radial orbital bias). To find the best Jeans model, we adjust the parameters of the dark halo.

The dark matter halos considered here (NFW and Burkert halos) are characterised by two parameters, a scale radius $r_{\rm dark}$ and a density $\varrho_{\rm dark}$. For a given tracer population and anisotropy β, we calculate a grid of models where the density acts as free parameter while the radii have discrete values, i.e. $r_{\rm dark} \in \{1, 2, 3, \ldots, 200\}$ kpc. The results of this modelling are summarised in Table 6, which quotes the best-fit halo parameters and the corresponding χ^2 values for the different tracer populations and anisotropies.

The confidence level (CL) contours are calculated using the definition by Avni (1976), i.e. using the difference $\Delta\chi^2$ above the minimum χ^2 value. With two free parameters, e.g. $(r_{\rm dark}, \varrho_{\rm dark})$ the 68, 90, and 99 per cent contours correspond to $\Delta\chi^2 = 2.30, 4.61$, and 9.21, respectively.

To facilitate the comparison of the results for the NFW halos to values in the literature, we use the equations given in Bullock et al. (2001) to express the $(r_{\rm s}, \varrho_{\rm s})$ pairs in terms of the virial parameters $(M_{\rm vir}, c_{\rm vir})$. These authors define the virial radius $R_{\rm vir}$ such that the mean density within this radius is $\Delta_{\rm vir} = 337$ times the mean density of the universe, and the concentration parameter is defined as $c_{\rm vir} = R_{\rm vir}/r_{\rm s}$. The confidence contours in Fig. 17 are shown in the $(M_{\rm vir}, c_{\rm vir})$ parameter space.

One immediately notices that the contours for the GCs (shown in the top and middle row of Fig. 17) are quite elongated, with a negative correlation between the virial mass and concentration. Below we discuss the results obtained for the different tracer populations.

10.2. NFW-models for the metal-rich population

The top row of Fig. 17 shows the NFW model parameters for the metal-rich (red) GCs. For a given value of β, the halos derived for the sample RIII (i.e. metal-rich GCs fainter than $m_R = 21.1$, after removal of GCs in the vicinity of NGC 1404 and the outlier-rejection as described in Sect. 5) are somewhat less massive and

Table 6. Jeans modelling best fit parameters.

			NFW dark halo							Burkert halo		
		β	r_s [kpc]	ϱ_S [$M_\odot$ pc^{-3}]	χ^2	χ^2/ν	M_{vir} [$10^{12} M_\odot$]	R_{vir} [kpc]	c_{vir}	r_0 [kpc]	ϱ_0 [$M_\odot$ pc^{-3}]	χ^2
	(1)	(2)	(3)	(4)	(5)	(6)	(7)	(8)	(9)	(10)	(11)	(12)
(*a*) NGC 1399 GC data (RIII and BIII):												
a1	Red (RIII)	−0.5	14	0.055	0.72	0.24	4.7	430	31	11	0.0896	0.49
a2	Red (RIII)	0	16	0.042	0.85	0.28	5.2	450	28	12	0.0776	0.57
a3	Red (RIII)	+0.5	24	0.019	1.02	0.34	7.9	490	20	16	0.0447	0.72
a4	Blue (BIII)	−0.5	101	0.00271	8.5	2.1	51	950	9	35	0.0213	6.9
a5	Blue (BIII)	0	174	0.00099	9.5	2.4	73	1075	6	46	0.0119	8.0
a6	Blue (BIII)	+0.5	≥200	0.00061	12	3.0	58	1000	5	94	0.0031	9.9
a7	$\text{Red}_{0.0}$ and $\text{Blue}_{0.0}$		63	0.0038	28	2.8	18	680	11	25	0.0237	28
a8	$\text{Red}_{+0.5}$ and $\text{Blue}_{-0.5}$		37	0.0110	29	2.9	13	610	16	20	0.0388	27
a9	$\text{Red}_{0.0}$ and $\text{Stars}_{0.0}$		23	0.0190	8.3	0.42	6.1	470	20	9	0.1343	14
a10	$\text{Red}_{0.0}$ and $\text{Stars}_{+0.5}$		34	0.0088	7.3	0.37	8.0	510	15	12	0.0728	8.7
(*b*) NGC 1399 GCs, extended data set including the Bergond et al. (2007) GC data (RV and BV):												
b1	Red (RV)	−0.5	12	0.093	3.8	0.63	5.4	450	38	9	0.166	3.4
b2	Red (BV)	0	14	0.069	4.0	0.67	6.1	470	34	11	0.112	3.5
b3	Red (BV)	+0.5	19	0.038	4.5	0.75	7.6	510	27	14	0.071	3.9
b4	Blue (BV)	−0.5	36	0.0140	14	2.0	17	660	18	22	0.0416	11
b5	Blue (BV)	0	50	0.0071	16	2.3	20	690	14	28	0.0243	13
b6	Blue (BV)	+0.5	94	0.0018	19	2.7	25	750	8	43	0.0094	16
b7	$\text{Red}_{0.0}$ and $\text{Blue}_{0.0}$		35	0.012	29	1.8	13	600	17	20	0.03876	27
b8	$\text{Red}_{+0.5}$ and $\text{Blue}_{-0.5}$		20	0.019	27	1.7	13	590	20	18	0.05124	24
b9	$\text{Red}_{0.0}$ and $\text{Stars}_{0.0}$		30	0.013	13	0.57	8.9	535	18	11	0.1064	19
b10	$\text{Red}_{0.0}$ and $\text{Stars}_{+0.5}$		38	0.0077	14	0.61	9.5	545	14	15	0.05653	14
(*c*) Stellar velocity dispersion profile (data from Saglia et al. 2000):												
c1	Stars	0	23	0.019	7.3	0.52	6.1	470	20	5	0.2996	10
c2	Stars	+0.5	47	0.0055	5.5	0.39	12	590	13	8	0.12545	7.5

Notes. Model identifiers: *(a)* using our GC dataset (i.e. samples RIII and BIII), *(b)* using the extended data set including the values from Bergond et al. (2007) (RV and BV), and *(c)* for the stellar velocity dispersion profile by Saglia et al. (2000). The tracer population is given in the first column, the anisotropy parameter β in the second. Columns 3 and 4 list the best-fit NFW halo parameters. The following columns give the χ^2 and χ^2/ν, where ν is the number of degrees of freedom (i.e. $k - 1 - p$, where k is the number of data points and $p = 2$ the number of free parameters). Columns 7–9 give the virial parameters of the dark halos, as defined by Bullock et al. (2001), i.e. assuming a density contrast of $\Delta = 337$. The parameters for the Burkert (1995) halo are shown in Cols. 10–12.

less concentrated than the halos found for the "extended" sample RV. The reason is that the latter includes bright GCs for which we found a larger velocity dispersion (e.g. Fig. 13, lower left panel). Note however that the models for RIII and RV agree within their respective 90% contours. The results also agree well with the halo parameters presented in Paper I (shown as a circle in Fig. 17).

The modelled dispersion profiles are compared to the observational data in the left and middle panel of Fig. 18. For both RIII and RV, the agreement between models and data is very good, and the best-fit models (shown as thin lines) for the different values of the anisotropy parameter β are indistinguishable. The model parameters listed in Table 6 illustrate the mass-anisotropy degeneracy, where the virial mass increases with β.

10.3. NFW models for the metal-poor GCs

The shape of the velocity dispersion profiles of the metal-poor GCs is not as smooth as that of the metal-rich GC population. The "jumps" in the profiles may be caused by the presence of interlopers. Since the dispersion values of adjacent bins show quite strong variations, the χ^2 values derived when modelling the blue GCs are substantially larger than those found for the red GCs.

The parameters derived for the sample BIII and the "extended" sample BV differ significantly: as can be seen from the middle row in Fig. 17, the solutions for the extended sample (solid contours) have a smaller virial mass and a larger concentration.

Compared to the models for the red GCs, the dark halos derived from the dispersion profile of the blue GCs are up to an order of magnitude *more massive* and about four times *less concentrated* which, as will be detailed below, considerably complicates the task of finding a common solution.

10.4. Finding joint solutions

Given that the different tracer populations (i.e. metal-rich and metal-poor GCs, and stars) move in the same potential, it is necessary to find a joint solution. For a set of tracer populations (labelled a and b), we determine the combined parameters by minimising the sum $\chi^2 = \chi^2_a + \chi^2_b$ in the $(r_{\rm dark}, \varrho_{\rm dark})$-parameter space. Since the tracer populations may have different orbital anisotropies, this procedure is performed for different combinations of β.

10.4.1. Combining red and blue GCs

First, we assume that $\beta = 0$ for both blue and red GCs. The dispersion profiles for the combinations BIII + RIII (model *a7*) and the "extended" samples BV + RV (model *b7*) are compared to the observations in the left and middle panel of Fig. 18,

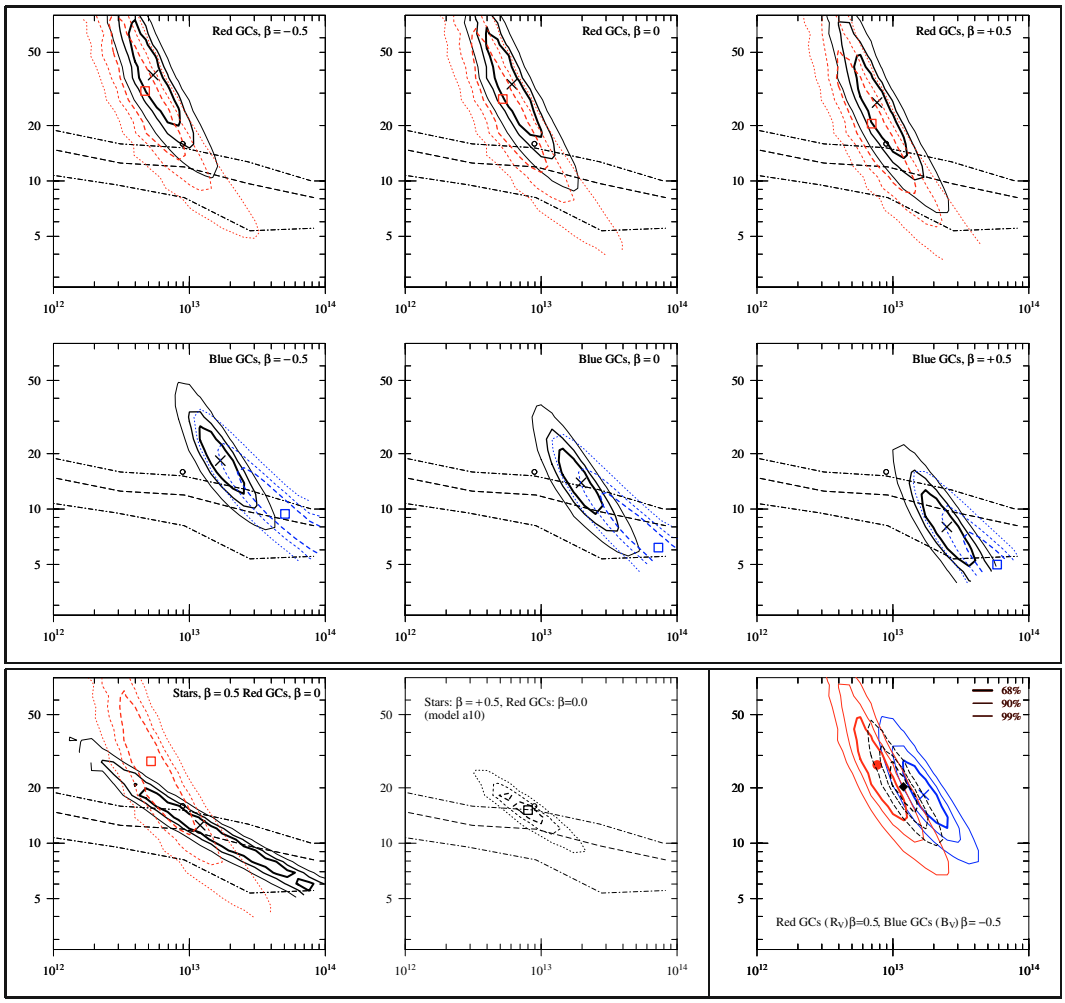

Fig. 17. Mass models (NFW halo): confidence level contours (68%, 90%, and 99%). The x-axis plots the virial mass ($M_{\rm vir}$, in units of $M_\odot$) and the y-axis is the dimensionless concentration parameter $c_{\rm vir}$. *Top row*: red GCs: from left to right, the panels display the results for $\beta = -0.5$, 0, and +0.5. Dashed contours show the values obtained for our GC data (RIII, models *a1* through *a3*), while the solid contours show the extended sample (RV, models *b1* through *b3*). The best-fit parameters for RIII and RV are marked by a square and a cross, respectively. *Middle row*: the same for the blue GCs: samples BIII (models *a4–a6*) and BV (models *b4–b6*). *Bottom left*: parameters of the NFW halo calculated from the stellar velocity dispersion of NGC 1399 as published by Saglia et al. (2000), assuming $\beta = +0.5$ (solid contours, model *c2*) compared to the red GCs RIII for $\beta = 0$ (dashed, model *a2*). The *bottom middle* panel shows model *a10*, the joint solution for the isotropic $\beta = 0$ red (RIII) and $\beta = +0.5$ stellar model shown in the *bottom left panel*. The *bottom right panel* illustrates the difficulty to find a common solution for red and blue GCs. Solid lines are the contours for $\beta = 0.5$ for red extended sample (RV centred on the dot) and for the blue GCs assuming $\beta = -0.5$ (sample BV, centred on the cross). The diamond indicates the joint solution, i.e. the minimum of $\chi^2_{\rm red} + \chi^2_{\rm blue}$. The corresponding contours are shown as dashed lines. Note that the best-fit joint solution lies *outside* the respective 68% CL contours of the individual GC tracer populations. In all panels, the long-dashed (dot-dashed) lines give the median (68 per cent values) for simulated halos as found by Bullock et al. (2001) (cf. their Fig. 4). For comparison, the circle ($M_{\rm vir} = 8.9 \times 10^{12}\,M_\odot, c_{\rm vir} = 15.9$) indicates the parameters of the best-fit NFW halo in Paper I. Note that the wiggles and gaps in the contours are an artifact of the finite grid-size and the re-gridding onto the ($M_{\rm vir}, c_{\rm vir}$)-plane.

respectively: the thick solid lines (labelled 7B and 7R for blue and red GCs, respectively) do not agree with the data in the sense that the models fail to reproduce the large difference one observes regarding the dispersions of red and blue GCs.

To find a better agreement between model and data, we combine the most massive halo found for the red GCs (i.e. $\beta_{\rm red} = +0.5$) with the least massive halo compatible with the blue GCs ($\beta_{\rm blue} = -0.5$).

The modelled dispersions for blue and red GCs are shown as thick dashed and long-dashed lines (labelled 8B and 8R) in the left and middle panel of Fig. 18. Again, the agreement between data and model is poor.

The bottom right panel of Fig. 17 shows the contours for this combination: the joint solution (shown as a diamond) for the blue "extended" sample (BV, $\beta = -0.5$) and the red sample (RV, $\beta = +0.5$) lies outside the 68% contour levels of the individual tracer populations.

10.4.2. Red GCs and the stellar velocity dispersion profile

The stellar velocity dispersion profile given by Saglia et al. (2000) is used to put constraints on the mass profile. To be consistent, we use the same stellar mass profile as for the calculations of the GC dispersion profiles (see Sect. 9.3). Since this profile is an approximation valid for $R \geq 500$ pc, we only consider the Saglia et al. data points outside 0.′15. The spatial density of the stars is given by Eqs. (13) and (14).

The detailed modelling by Saglia et al. (2000) revealed that the stars have a radially variable anisotropy parameter $\beta(R)$, which is positive and almost reaches $\beta = +0.5$ near $\sim 10''$

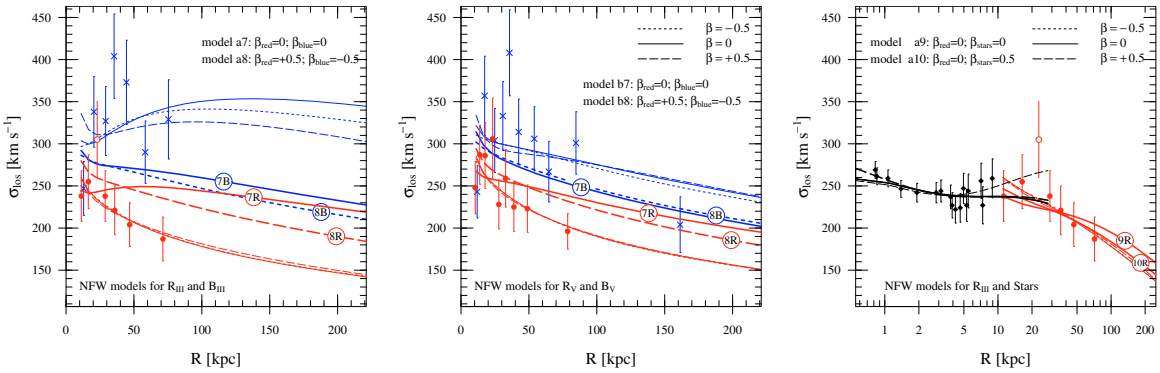

Fig. 18. Best fit Jeans models (NFW halo). *Left panel*: NGC 1399 GC data and modelled velocity dispersion profiles. Crosses and dots show the red (RIII) and blue (BIII) velocity dispersion profiles (for a moving bin of 35 GCs, cf. Fig. 13, lower panels), respectively. The *thin* curves are the best fit models obtained for the red (models *a1–a3*) and the blue GCs (models *a4–a6*) separately. The *thick* lines (with labels) show the dispersions for the combined model for red and blue GCs (models *a7* and *a8*). *Middle panel*: the same for the "extended" samples including the Bergond et al. (2007) measurements (samples RV and BV). *Right panel*: red GCs and stars. Diamonds show the stellar velocity dispersion (Saglia et al. 2000), the red GCs (RIII) are shown as dots. The thin lines are the models for the individual tracer populations, i.e. models *c1* and *c2* for the stars and models *a1–a3* for the red GCs. The thick curves are the joint solutions, i.e. models *a9* and *a10*. In all panels, solid lines are isotropic models, and the models with $\beta = -0.5$ and $\beta = +0.5$ are shown as dashed and long-dashed lines, respectively. The parameters of the halos shown here are listed in Table 6.

(see their Fig. 5). We therefore model the stars for the constant anisotropies $\beta = 0$ and $\beta = +0.5$ (models *c1* and *c2*, respectively). The model with the radial bias gives a slightly better fit to the data. The stellar data cover the central ∼10 kpc, i.e. a region with $R \leq r_s$. Thus, the scale radius and hence the total mass of the dark halo cannot be constrained by these data. However, as can be seen from the bottom left panel in Fig. 17 (solid contours) the concentration parameter c_{vir} is quite tightly constrained. The contours for the red GCs (sample RIII, $\beta_{red} = 0$) shown in the same panel (dashed contours) have a substantial overlap with the parameter space allowed by the stars. The contours for the joint solution (model *a10*) are shown in the bottom middle panel of Fig. 17.

The corresponding models are compared to the observed velocity dispersion profiles in the right panel of Fig. 18. The thick line labelled "10R" shows the joint solution for the red GCs and the thick long-dashed line shows the corresponding model for the stars. For stars and red GCs alike the agreement between the combined model (a10) and the data is excellent, and we adopt this solution (which also agrees very well with the result from Paper I) as our preferred mass model for NGC 1399. The NFW halo has a scale parameter of $r_s = 34$ kpc, a density $\varrho_s = 0.0088\, M_\odot\, pc^{-3}$, and the virial radius is $R_{vir} = 510$ kpc.

10.5. Jeans models for a cored halo

We now assume that the cumulative mass of the dark halo is described by the expression given in Eq. (22). This cored halo, introduced by Burkert (1995), has two free parameters as well, namely the central density ϱ_0 and the scale radius r_0. The solutions of the Jeans equation are found in the same manner as outlined in Sect. 10.1, with the radii being fixed to values $r_0 \in \{1, 2, 3, \ldots 100\}$ kpc.

The best-fit parameters are given in the last columns of Table 6.

Again, the solutions found for the red GCs have substantially smaller scale-radii than the halos describing the blue GCs. For a given tracer population, the cored halo models provide a fit of similar quality, and we compare the derived mass profiles in Fig. 19. We find that for a given dispersion profile the Burkert halos are less massive than the corresponding NFW halos. Within the central ∼80 kpc, which is about the radial extent of the data sets RIII and BIII, however, the corresponding mass profiles are almost indistinguishable.

11. Discussion

The strongest evidence pointing towards the existence of substructure within the GCSs of elliptical galaxies is the bimodal distribution of GC colours. The works by e.g. Kundu & Whitmore (2001a,b); Larsen et al. (2001) and Peng et al. (2006) confirmed that colour bimodality is a ubiquitous feature in the GCS of giant ellipticals. As opposed to the Milky Way, where the GC metallicity can be directly measured from spectra of individual GC stars and the presence of kinematically distinct subpopulations has been firmly established (e.g. Zinn 1985; Côté 1999), there are but very few spectroscopic metallicity measurements for GCs surrounding giant elliptical galaxies (e.g.Cohen et al. 1998, 2003 for M 87 and M49, respectively). Thus, the interpretation of the *colour bimodality* of elliptical galaxies in terms of a bimodal *metallicity* distribution, as proposed by e.g. Ashman & Zepf (1992), has not gone unchallenged: the fundamental question in this respect is whether the description as two separate populations is true or whether we rather face a continuum of properties where the bimodal appearance is just a morphological feature in the colour distribution, caused by a non-linear colour-metallicity relation (e.g. Richtler 2006; Yoon et al. 2006).

That in NGC 1399 blue and red GCs show a distinct dynamical behaviour was already shown in Paper I. To gain a more quantitative understanding of the kinematical differences between blue and red GCs, we plot in Fig. 20 the velocity dispersion as function of $C - R$-colour. Our sample shows a jump in the velocity dispersion at $C - R \simeq 1.55$ rather than a velocity dispersion which smoothly changes with colour. In the case of elliptical galaxies, this has not yet been shown before and it is clear evidence that we indeed face two different populations.

11.1. Population aspects

It is clear however that a simple colour cut does not cleanly separate these two populations, but that there is some contamination of the blue population by members of the red population and

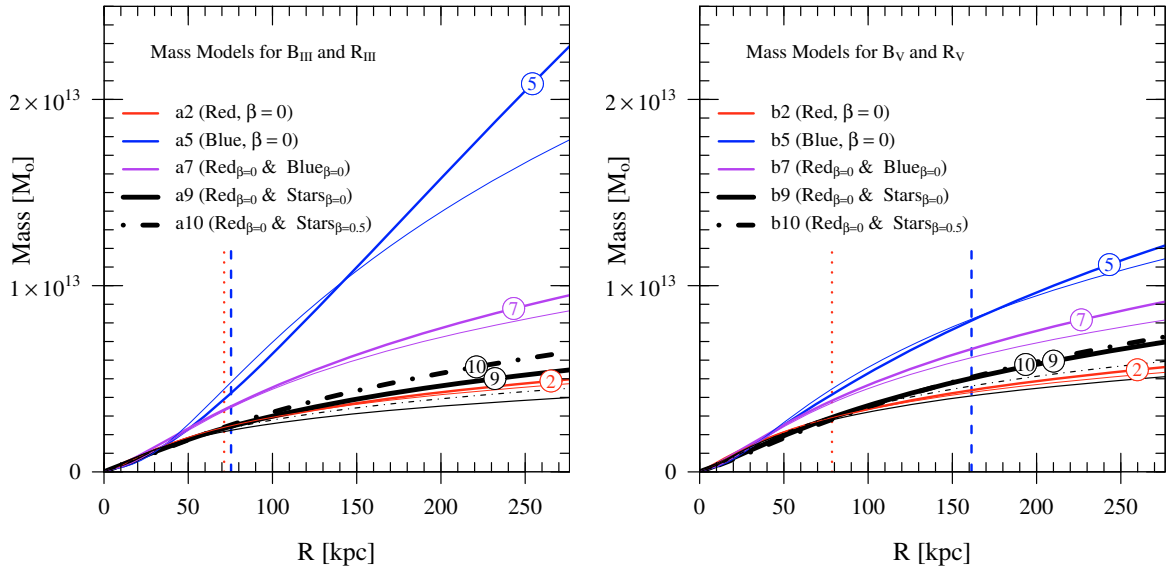

Fig. 19. *Left panel*: mass profiles derived for the GC dispersion profiles RIII and BIII. The thick lines with labels referring to the identifiers in Table 6 show the mass assuming an NFW-type dark halo. The cored Burkert halos are shown as thin curves with the same line style. For a given tracer population, the Burkert halo is less massive than the best-fit NFW halo. *Right panel*: the same for the extended data sets RV and BV (i.e. including velocities from B+07). In both panels, the dotted and dashed vertical lines indicate the radial distance of the outermost velocity dispersion data point for the red and blue GCs, respectively (cf. Table A.2).

vice versa. Intrinsically, these populations are expected to differ more strongly in their kinematical and structural properties than our observationally motivated blue and red populations.

Motivated by this strong evidence for two dynamically distinct subpopulations in the NGC 1399 GCS, we now address the question concerning the nature and origin of the blue (metal-poor) and red (metal-rich) GCs in NGC 1399.

In the following, we discuss the idea that a major part of the GCS, namely the blue GCs, has its origin predominantly in the accretion of material, supposedly in the form of dwarf galaxies, during the assembly of NGC 1399 and the entire Fornax cluster.

This concept is not at all new (Côté et al. 1998; Hilker et al. 1999) but our large sample enables us to distinguish the two subpopulations better than it was previously possible.

The comparison with the Galactic GCS is instructive. The picture of the Milky Way's halo has undergone a dramatic change from an homogeneous stellar distribution to a strongly sub-structured halo (see the review article by Helmi 2008). The Sagittarius dwarf donated six GCs to the Galactic system (e.g. Bellazzini et al. 2003). The extragalactic origin of ω Centauri as a former nucleus of a dwarf galaxy is hardly doubted any more (Hilker & Richtler 2000; Hilker et al. 2004; Bedin et al. 2004; Villanova et al. 2007), and many of the Galactic halo GCs with anomalous horizontal branches (HBs) are suspected to have their origin outside the Milky Way (Lee et al. 2007; Catelan 2009).

Given the many tidal streams detected (and yet to be detected), the hypothesis that a large part of the Galactic halo has fallen in has strong arguments in its favour. If this applies to a relatively isolated spiral galaxy, we would expect the effects of accretion to be much more important in a giant elliptical in the centre of an assembling galaxy cluster.

11.1.1. Red GCs

The metal-rich GCs resemble the stellar field population of NGC 1399 under various aspects: the density profiles (shown in Fig. 15) and the velocity dispersions (Fig. 14, upper panel) are indistinguishable in the radially overlapping domain. Further, the field population and the red GCs show similar anisotropies in terms of h_4 and κ, respectively. This strongly points towards a common formation history. This is further supported by the spatial distribution of red GCs in elongated galaxies, which closely follows the galaxy light, (e.g. NGC 1380 Kissler-Patig et al. 1997; NGC 1052 Forbes et al. 2001b).

Currently, the mechanisms leading to the assembly of the giant ellipticals which now reside at the centres of galaxy clusters are not fully understood and a matter of debate (e.g. Collins et al. 2009; Colavitti et al. 2009 and references therein). The very old stellar ages derived for giant ellipticals (e.g. Trager et al. 2000) point towards their formation at high redshift followed by passive evolution with no major episodes of star formation (or GC formation, see below). Such an early assembly is, for instance, an inherent feature of the "revised monolithic collapse scenario" by Pipino et al. (2008).

According to the available observational evidence, GC formation is enhanced in regions of high star formation rate (Larsen & Richtler 2000; Weidner et al. 2004; Schweizer 2006). In the case of NGC 1399, the first epoch of massive cluster formation was supposedly during the first major merger or the collapse phase assembling the main body of NGC 1399. As can be seen from on-going mergers (e.g. Whitmore & Schweizer 1995; Wang et al. 2004), the starburst commences well before the components are actually merged (for theoretical models see e.g. Mihos & Hernquist 1996 and di Matteo et al. 2008). Thus, also in the merger scenario, one expects the formation of metal-rich GCs at a quite early stage. The processes leading to equilibrium, whether it is phase mixing or violent relaxation, then act equally on the stellar field population and the metal-rich GCs, leaving the same imprints on both populations. However, the same processes which lead to the observed similarities between the field stars and the metal-rich GCs also erased all dynamical traces from the epoch when the GCs were formed – thus rendering the distinction between a monolithic collapse scenario and a series of (early) gas-rich mergers impossible. In their very deep images of NGC 1399 Tal et al. (2009) did not find any of the classical merger signatures (i.e. shells, isophotal twists, tidal

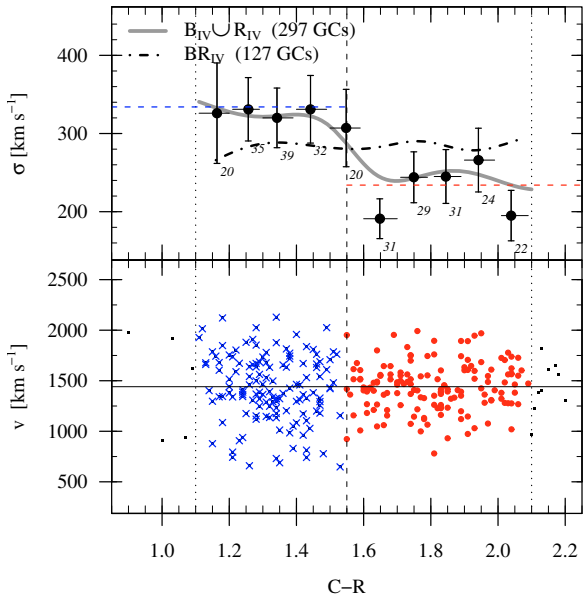

Fig. 20. *Upper panel*: velocity dispersion as a function of $C - R$-colour. The data points show the velocity dispersion for the Class A GCs which are fainter than $m_R = 21.1$ (i.e. the union of samples BIV and RIV) for bins of 0.1 mag width. The labels show the number of GCs in a given bin. For bins containing less than 10 GCs, no dispersion was calculated. The dashed horizontal lines are the velocity dispersions of the samples BIV and RIV as given in Table 3. The solid curve shows the dispersion calculated using a Gaussian kernel with $\sigma = 0.1$ mag. For comparison, the dot-dashed curve shows the same for the bright Class A GCs (sample BRIV). *Lower panel*: velocities vs. colour. Crosses and dots show blue and red GCs (from the samples BIV and RIV, respectively) used in the upper panel. Small squares indicate GCs in the too sparsely populated colour bins. In both panels, the dashed line at $C - R = 1.55$ indicates the colour used in this work to divide blue from red GCs. The vertical dotted lines indicate the colour range for which the dispersions are calculated.

tails, plumes and fans) – which further points towards an early assembly of NGC 1399 and its predominantly old (Kissler-Patig et al. 1998; Forbes et al. 2001a; Kundu et al. 2005; Hempel et al. 2007) metal-rich GCs.

11.1.2. Blue GCs

The blue GCs are distinguished from their red counterparts by a shallower density profile and a higher velocity dispersion. It had been concluded in Paper I that the difference in the density profile would be enough to explain the difference in the velocity dispersion profile. Our present treatment, however, differs from the one in Paper I. Firstly, we do not impose such a strict velocity cut. Secondly, we use an updated density profile which is steeper for large radii. Because of these factors, finding a halo which simultaneously satisfies the constraints from the red and the blue GCs is more difficult.

Moreover, the fluctuations of the velocity dispersion on small radial scales are larger than one would expect from Poissonian noise alone. The velocity uncertainties of the blue GCs are admittedly larger but this feature persists also after imposing a quality selection.

In Paper I, we identified a set of predominantly blue GCs with extreme velocities and showed that their apogalactic distances must be about 500−700 kpc, i.e. significantly larger than the traceable extent of the NGC 1399 GCS, or the core of the Fornax cluster which both are of the order ∼250 kpc (Bassino et al. 2006 and Ferguson 1989, respectively).

To explain the complex kinematical properties of the metal-poor GCs, we propose a scenario in which the majority of the blue GCs surrounding NGC 1399 belong to this galaxy's very extended GCS as suggested by Schuberth et al. (2008). In addition, there is a population of "vagrant" GCs which formerly belonged to (i) dwarf galaxies (which were disrupted in the encounter with NGC 1399) or (ii) one of the more massive early-type galaxies in the Fornax cluster core: while the large relative velocities of the galaxies near the cluster centre make mergers very unlikely (compared to group environments where the velocity dispersion is smaller), the fly-by of a galaxy might lead to tidal stripping of GCs (Forbes et al. 1997; Bekki et al. 2003). Since, in general, the metal-poor GCs have a shallower number density distribution than the metal-rich GCs, the former are more likely to get stripped. The observed kinematic properties of these stripped GCs would depend strongly on the orientation of the "donor" galaxy's orbit with respect to the plane of the sky and, of course, the impact parameter and the effectiveness of the stripping.

Assuming that the stripped GCs would form a stream which roughly follows the donor's orbit, GCs stripped in a galaxy-galaxy encounter taking place in the plane of the sky would be next to undetectable since their velocities would be very close to the systemic velocity.

For a galaxy such as NGC 1404, on the other hand, which has a large relative velocity (and there are signs that its orbit is very inclined, cf. Machacek et al. 2005), one would expect the stripped GCs to have extreme velocities.

In this picture, the observed velocity field of the blue GCs is the superposition of a dynamically old population and streams of GCs whose phase-space coordinates are still correlated with the orbits of the donor galaxies. Depending on the geometry, the observed line-of sight velocity dispersion derived from this composite distribution can easily exceed the intrinsic dispersion of the dynamically old GCs belonging to NGC 1399 itself.

However, as pointed out in Sect. 5.2, a robust test of this scenario requires a more complete spatial coverage than provided by our current data set in conjunction with numerical simulations. Assuming that the contamination by stripped GCs is indeed the cause for the jagged appearance of the line-of-sight velocity dispersion profile of the NGC 1399 blue GCs (cf. Fig. 13, right panels), one would expect the dispersion profiles of blue GCs of ellipticals residing in lower density environments to be more regular. NGC 4636 is such a galaxy: it is situated in the very outskirts of the Virgo cluster (its nearest giant neighbour has a projected distance of ∼175 kpc) and Tal et al. (2009) found no signs for a (recent) merger. Aside from two blue GCs with extreme velocities, the quality-selected velocity dispersion profile of the metal-poor GCs declines and has a smooth appearance (Schuberth et al. 2006, 2009 in prep.).

11.2. Dynamical aspects

In the following, we discuss the stellar-dynamical quantities and compare the derived mass profiles to the results from X-ray studies and cosmological N-body simulations.

11.2.1. Rotation

So far, no clear picture regarding the rotational properties of the GCSs of giant ellipticals has emerged. For instance, M 87 shows

significant rotation for both the metal-rich and the metal-poor GCs, albeit with different axes of rotation (Côté et al. 2001). In NGC 4472, only the metal-poor GCs show a strong rotation signal (Côté et al. 2003). For NGC 4636, no rotation is detected for the metal-poor GCs, while there are indications for a rotation of metal-rich GCs (Schuberth et al. 2006) (for an overview and discussion of the rotational behaviour of the GCSs of several elliptical galaxies see Romanowsky et al. 2009).

In the case of NGC 1399, we find no rotation signal for the red (metal-rich) GCs. This is in agreement with the findings for the field population for which Saglia et al. (2000) quote an upper limit of $v_{\rm rot} \simeq 30\,{\rm km\,s^{-1}}$. For the blue GCs, however, the situation is more complicated: although the (∼95% CL) rotation signature found for the entire blue sample (BI, for the full radial range) vanishes when culling the more uncertain (Class B) velocity measurements from the analysis (sample BIV), the rotation signal for the radial range $4' < R \leq 8'$ ($22 \lesssim R \lesssim 44$ kpc, i.e. the outer subsamples) appears to be robust with respect to interloper removal and quality selection. The values (after interloper removal; $A = 110 \pm 53$ km s^{-1}, $\Theta_0 = 130 \pm 53°$) are consistent with the rotation signature reported in Paper I.

Unfortunately, for the outermost parts ($R \gtrsim 50$ kpc) of the NGC 1399 GCS where, according to numerical simulations (Bekki et al. 2005), the rotation amplitude of the metal-poor GCs is expected to be largest, the data suffer from a very incomplete angular coverage, thus precluding any statement regarding the rotation of the GCS at very large galactocentric distances.

11.2.2. Comparison to cosmological simulations

In Fig. 18 we compare our solutions to the results presented in the study of Bullock et al. (2001) (cf. their Fig. 4). These authors analysed a sample of ∼5000 simulated halos with virial masses in the range 10^{11}–$10^{14}\,M_\odot$. The concentration parameter $c_{\rm vir} \equiv R_{\rm vir}/r_{\rm dark}$ decreases with growing halo mass (solid line). The scatter in this relation, however, is quite large, as the dashed lines encompassing 68 per cent of the simulated halos show.

We find that our best-fit combined halos with $r_{\rm dark} \simeq 30$ kpc have somewhat higher concentrations than simulated halos of a similar mass. Yet one has to bear in mind that the numerical experiments were carried out using dark matter particles only. It is conceivable that the presence of baryons and dissipative effects might act to increase the concentration of real halos. Thus we conclude that our best-fit halos do not stand in stark contrast to the halos found in cosmological N-body simulations.

11.3. Comparison with X-ray mass profiles

NGC 1399 and the Fornax cluster have, due to their proximity and brightness, been extensively observed by several X-ray satellite missions, and the data support the existence of a massive dark halo (e.g. Jones et al. 1997; Ikebe et al. 1996, and Paolillo et al. 2002). Recently, Churazov et al. (2008) used Chandra data to demonstrate that, for the central 4.′5 (≃25 kpc), the gravitational potentials derived from stellar kinematics (cf. Saglia et al. 2000) and X-rays agree very well. Regarding larger scales, the Fornax cluster is known to be morphologically quite complex: for example, Ikebe et al. (1996), using ASCA data, reported the discovery of substructure in the X-ray maps which they interpreted in terms of a galaxy-sized dark halo embedded in a cluster-wide halo.

Using deep high-resolution ROSAT data, Paolillo et al. (2002) confirmed this finding and identified three different structures: the innermost component is centred on NGC 1399 and dominates the inner 50″(≃4.6 kpc). Then follows a second, almost spherical "galactic halo" component, the centre of which lies 1′ SW of NGC 1399, its radial extent is of the order 400″(≃ 35 kpc). The third and most extended "cluster" component is more elongated and its centre lies 5.′6 northeast of NGC 1399.

In terms of the total mass profile, the existence of different components leads to "shoulder-like" features near the interface regions (i.e. where the gas-densities of two components become equal). This behaviour is clearly seen for the range of mass-profiles derived in both studies, see Fig. 17 of Paolillo et al. (2002) for a comparison.

Makishima et al. (2001) who analysed a sample of 20 galaxy clusters (including Fornax and Virgo) propose that such hierarchical dark matter profiles, parametrised in terms of a central excess mass superimposed on a cored King-type profile, are in general linked to the presence of a cD galaxy. Cuspy profiles, on the other hand, are found in the absence of a cD galaxy (e.g. Abell 1060 which has two central giant ellipticals).

In the case of NGC 1399, the transition from the central component to the cluster-wide component takes place at about 60 kpc (≃11′), a region probed by our GC sample.

The question arises, accordingly, which consequences such a "nested" mass distribution would have on the GC dynamics. Would one be able to detect signs of such a halo-in-halo structure in the velocity dispersion profile of the GCs?

We chose the isothermal profile of Ikebe et al. (their Model 1) and, using the standard β-model for the X-ray gas density profiles

$$\varrho_{\rm gas}(r) = \varrho_{\rm gas,0}\left(1 + \frac{r^2}{r_{\rm c}^2}\right)^{-\frac{3}{2}\beta_X}, \tag{23}$$

calculate the total gravitating mass using

$$M(<r) = \frac{-kT}{G\mu m_{\rm H}}\left(\frac{{\rm d}\ln\varrho}{{\rm d}\ln r} + \frac{{\rm d}\ln T}{{\rm d}\ln r}\right) r \tag{24}$$

(Fabricant et al. 1980). Here, β_X is the power-law exponent, $m_{\rm H}$ is the mass of the hydrogen atom, and $\mu = 0.6$ the mean molecular weight (assuming a fully ionised plasma with primordial element abundances). The total density is the sum of two components with the parameters given in Table 1 of Ikebe et al.: $\varrho_{1,0} = 2.3 \times 10^{-2}\,{\rm cm^{-3}}$, $\varrho_{2,0} = 8.2 \times 10^{-4}\,{\rm cm^{-3}}$, $r_{c,1} = 4.8$ kpc $r_{c,2} = 127$ kpc, $\beta_{X,1} = 0.51$, and $\beta_{X,2} = 0.60$. Since we assume that the gas is isothermal ($T = 1.2 \times 10^7$ K), the second term in Eq. (24) vanishes. Figure 21 shows the velocity dispersion profiles expected for the blue and red GC subpopulations (assuming constant anisotropy parameters of $-0.5, 0, +0.5$) for the mass profile given in Eq. (24) and plotted in Fig. 22. Indeed, the modelled velocity dispersion profiles show a dip near ∼40 kpc, but the feature is quite shallow and appears to be at variance with the findings for the red GCs.

The mass profiles derived by Paolillo et al. (2002) would lead to more pronounced features in the predicted velocity dispersion profiles. Note however that a simple isothermal profile based on the gas density distribution ignoring the offsets of the different components (shown as thick line in their Fig. 15) leads to a non-monotonic (i.e. unphysical) density-profile at the transition from the galaxy to the cluster component.

Figure 22 compares the mass profiles derived in this study (shown as solid and dot-dashed lines) with the X-ray mass profiles presented by Paolillo et al. (2002) and Ikebe et al. (1996).

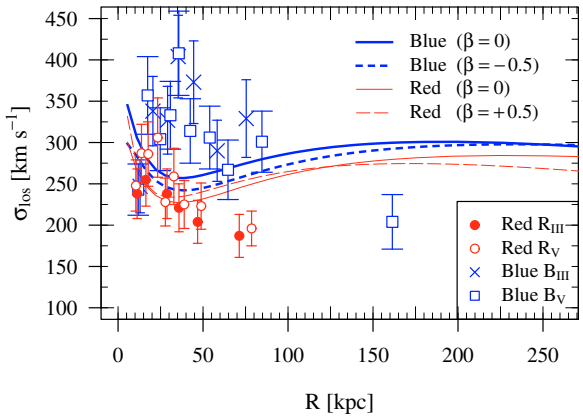

Fig. 21. Comparison to the "nested halo" mass profile by Ikebe et al. (1996). Here, we plot the dispersion profiles expected for their Model 1, see text for details. The thick curves are the dispersion profiles for the blue GCs, where the solid and dashed lines correspond to $\beta = 0$ and $\beta = -0.5$, respectively. The thin lines show the models for the red GCs. The solid line is $\beta = 0$, and the long-dashed line shows the model for $\beta = +0.5$. The data for the red GC samples RIII and RV are shown as dots and circles, respectively. The corresponding blue samples BIII and BV are shown as crosses and unfilled squares, respectively.

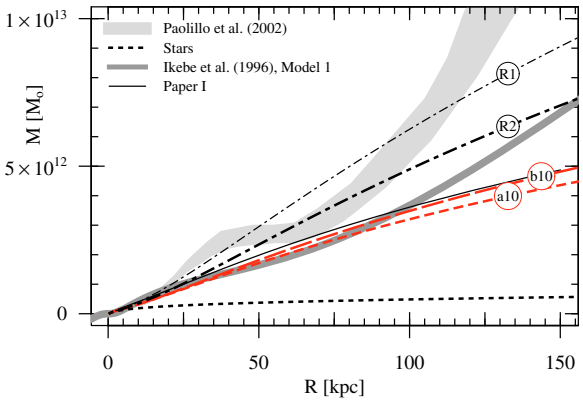

Fig. 22. Comparison to X-ray measurements. The grey area shows the range of the mass models presented by Paolillo et al. (2002). The thick solid line shows the mass derived by Ikebe et al. (1996) (their Model 1). The thin solid line indicates the mass profile derived in Paper I. The dash-dotted curves are the two halos presented in Richtler et al. (2008): the more massive one (labelled R1) has the parameters $r_s = 50$ kpc and $\varrho_s = 0.0085\, M_\odot\,\mathrm{pc}^{-3}$. The halo derived for the "safe" sample in Richtler et al. (2008) (R2) has $r_s = 50$ kpc and $\varrho_s = 0.0065\, M_\odot\,\mathrm{pc}^{-3}$. The dashed and long-dashed curves are the best-fit NFW mass profiles *a10* and *b10* derived in this work (cf. Table 6). The stellar mass is shown as a short-dashed line.

Within the central 100 Mpc, where the vast majority of our dynamical probes is found, the preferred mass profiles derived in this study agree well with the Ikebe et al. (1996) mass model, although we do not find any signs for the transition from galaxy to cluster halo in our kinematic data.

12. Conclusions

Using the largest data set of globular cluster (GC) radial velocities available to date, we revisit and extend the investigation of the kinematical and dynamical properties of the NGC 1399 GC system with respect to Richtler et al. (2004, Paper I). We measure about 700 GC radial velocities out to approximately $14.5' \simeq 80$ kpc (in Paper I we reached 40 kpc). To this sample we add 56 GC velocities from Bergond et al. (2007, B+07) which go as far out as 200 kpc.

Our main findings are the following: there is no significant rotation signal among the red (metal-rich) subpopulation. We find rotation around the minor axis for the blue (metal-poor) clusters in a radial interval of $4' < R < 8'$ (i.e. 22 kpc $\lesssim$ R $\lesssim$ 44 kpc), however weak. The blue and red clusters form two *kinematically distinct* subpopulations rather than showing a continuum of kinematical properties.

The red clusters correspond under various kinematical aspects to the stellar field populations.

Their velocity dispersion declines outwards and their velocity distribution suggests orbital isotropy.

The jump to the higher dispersion of the blue clusters occurs at a colour ($C-R = 1.55$), which is also suggested by the morphology of the colour distribution. The blue GCs, however, show a more complex behaviour. Their velocity dispersion profile is not as smooth as that of the red GCs. There exist very high/low individual velocities, which suggest very large apogalactic distances, as already found in Paper I. These objects seem to belong to an intergalactic cluster population, which may be made up of GCs stemming from disrupted dwarfs and GCs stripped off neighbouring galaxies during close encounters.

We performed a Jeans analysis in order to constrain the mass profile (stellar plus dark). We found it difficult to find a dark halo which simultaneously accounts for the red and the blue clusters, which again argues for a different dynamical history.

The dark NFW-halo which was found to represent the kinematics of the red GCs ($\beta_{\mathrm{GCs}} = 0$) and the stellar velocity dispersion profile presented by Saglia et al. (2000) ($\beta_{\mathrm{stars}} = +0.5$), our Model *a10*, has the parameters $\varrho_{\mathrm{dark}} = 0.0088\, M_\odot\,\mathrm{pc}^{-3}$ and $r_{\mathrm{dark}} = 34$ kpc. The virial mass is $M_{\mathrm{vir}} = 8.0 \times 10^{12}\, M_\odot$.

Including the velocities from B+07, (Model *b10*) yields a slightly more massive halo ($\varrho_{\mathrm{dark}} = 0.0077\, M_\odot\,\mathrm{pc}^{-3}$ and $r_{\mathrm{dark}} = 38$ kpc, and a virial mass $M_{\mathrm{vir}} = 9.5 \times 10^{12}\, M_\odot$).

These NFW halos, which were found to represent the observations, are marginally less massive than the one from Paper I. The total mass profile fits agree reasonably well with the X-ray based mass profiles out to 80 kpc. However, our model halos when extrapolated stay significantly below the X-ray masses. Moreover, we do not see the transition from the galaxy halo to the cluster halo claimed to be present in the X-ray data.

We argue that these findings are consistent with a scenario where the red GCs are formed together with the bulk of the field population, most probably in early multiple mergers with many progenitors involved. This is consistent with the NGC 1399 GCs being predominantly old (Kissler-Patig et al. 1998; Forbes et al. 2001a; Kundu et al. 2005; Hempel et al. 2007), with ages very similar to the stellar age of NGC 1399 (11.5 ± 2.4 Gyr, Trager et al. 2000)

A large part of the blue GC population has been acquired by accretion processes, most plausibly through dwarf galaxies during the assembly of the Fornax cluster. Moreover, there should be a significant population of intra-cluster GCs.

Acknowledgements. We thank the anonymous referee for helpful comments. We also thank Mike Fellhauer for fruitful discussions. Y.S. acknowledges support from a German Science Foundation Grant (DFG-Projekt HI-855/2). T.R. and A.J.R. acknowledge support from the Chilean Center for Astrophysics, FONDAP No. 15010003. A.J.R. was further supported by the National Science Foundation grants AST-0507729 and AST-0808099. This research has made use of the NASA/IPAC Extragalactic Database (NED) which is operated by the Jet Propulsion Laboratory, California Institute of Technology, under contract with the National Aeronautics and Space Administration.

Appendix A: Radial velocity dispersion profiles

Table A.1. Velocity dispersion profiles for fixed annular bins (cf. Fig. 13, middle panels).

Blue (metal-poor) GCs						Red (metal-rich) GCs					
Bin	$\bar{R}$	$\sigma_{\rm los}$	$\Delta\sigma_{\rm los}$	$N_{\rm gc}$	$\bar{v}$	Bin	$\bar{R}$	$\sigma_{\rm los}$	$\Delta\sigma_{\rm los}$	$N_{\rm gc}$	$\bar{v}$
(1)	(2)	(3)	(4)	(5)	(6)	(1)	(2)	(3)	(4)	(5)	(6)
Sample BI						Sample RI					
1	2.59	288	30	50	1398	1	2.47	244	22	68	1446
2	4.59	312	35	42	1440	2	4.52	278	27	64	1461
3	6.43	396	36	61	1459	3	6.40	244	26	47	1450
4	8.52	363	46	33	1488	4	8.42	260	35	36	1556
5	11.06	351	39	42	1447	5	11.07	282	41	27	1425
6	13.77	369	58	22	1332	6	13.69	–	–	7	1222
7	17.02	–	–	6	2101	7	16.10	–	–	7	1463
Sample BII						Sample RII					
1	2.59	288	30	50	1398	1	2.47	244	22	68	1446
2	4.59	312	35	42	1440	2	4.52	278	27	64	1461
3	6.39	393	37	58	1387	3	6.40	244	26	47	1450
4	8.53	350	46	30	1444	4	8.41	216	30	28	1504
5	11.06	325	38	38	1412	5	11.09	281	41	26	1422
6	13.77	369	58	22	1332	6	13.69	–	–	7	1222
7	17.02	–	–	6	2101	7	16.10	–	–	7	1463
Sample BIII						Sample RIII					
1	2.59	288	30	50	1398	1	2.47	244	22	68	1446
2	4.59	312	35	42	1440	2	4.52	278	27	64	1461
3	6.39	393	37	58	1387	3	6.40	225	25	46	1461
4	8.53	350	46	30	1443	4	8.41	216	30	28	1504
5	11.02	296	36	37	1395	5	11.13	188	30	23	1418
6	13.76	338	58	21	1320	6	13.69	–	–	7	1222
7	17.56	–	–	2	1471	7	16.10	–	–	7	1463
Sample BIV						Sample RIV					
1	2.62	234	33	27	1411	1	2.45	260	30	42	1398
2	4.48	317	47	24	1445	2	4.57	256	29	43	1467
3	6.37	371	43	38	1478	3	6.43	209	27	32	1428
4	8.52	375	62	19	1466	4	8.38	206	32	22	1485
5	11.01	351	59	20	1363	5	10.93	167	33	14	1392
6	13.87	338	88	11	1343	6	13.18	–	–	4	1208
7	–	–	–	0	–	7	15.57	–	–	1	1485
Sample BV						Sample RV					
1	2.56	303	28	64	1398	1	2.44	280	21	97	1405
2	4.56	317	32	53	1494	2	4.55	265	22	80	1454
3	6.40	369	31	73	1386	3	6.44	245	23	63	1472
4	8.51	325	40	35	1486	4	8.38	220	29	32	1488
5	11.10	271	27	53	1429	5	11.04	213	29	29	1418
6	13.75	322	45	28	1380	6	13.80	190	43	14	1366
7	21.66	254	40	21	1424	7	19.33	107	23	13	1463
8	34.75	136	31	10	1466	8	–	–	–	–	–

Notes. The bins start at $R = 1\farcm0, 3\farcm5, 5\farcm5, 7\farcm5, 9\farcm5, 12\farcm5, 15\farcm5$, and $30\farcm0$; at a distance of 19 Mpc, $1\farcm0$ corresponds to 5.2 kpc. The left and right table show the values obtained for the blue and red GCs, respectively. The Roman numerals refer to the sample definition in Sect. 5.4. Column (1) gives the bin number, the mean radius of the GCs in a bin is given in Col. (2). The velocity dispersion (in units of km s^{-1}) and its uncertainty are given in Cols. (3) and (4). Column (5) is the number of GCs in a given bin, and Col. (6) their mean velocity.

Table A.2. Velocity dispersion profiles for the subsets of our data used for the Jeans modelling.

N°	$\bar{R}_{\rm blue}$ [arcmin]	$\sigma_{\rm blue}$ [km s^{-1}]	$\Delta\sigma_{\rm blue}$ [km s^{-1}]	$N_{\rm GC}$	$R_{\rm min}$ [arcmin]	$R_{\rm max}$ [arcmin]	$\bar{v}$	$\bar{R}_{\rm red}$ [arcmin]	$\sigma_{\rm red}$ [km s^{-1}]	$\Delta\sigma_{\rm red}$ [km s^{-1}]	$N_{\rm GC}$	$R_{\rm min}$ [arcmin]	$R_{\rm max}$ [arcmin]	$\bar{v}$ [km s^{-1}]
Blue GCs (sample BIII)								Red GCs (sample RIII)						
1	2.34	247	32	35	1.72	2.83	1406	2.03	238	29	35	1.12	2.43	1450
2	3.71	338	42	35	2.90	4.63	1400	2.96	255	32	35	2.45	3.53	1427
3	5.27	327	40	35	4.63	5.82	1465	4.15	305	44	35	3.53	4.69 (⋆)	1562
4	6.40	404	49	35	5.82	7.08	1455	5.21	238	30	35	4.74	5.82	1436
5	8.05	373	46	35	7.08	9.14	1397	6.48	221	29	35	5.84	7.31	1496
6	10.55	290	36	35	9.24	11.66	1414	8.47	204	26	35	7.40	9.95	1451
7	13.65	329	46	30	11.70	18.24	1364	12.90	187	25	33	10.10	16.98	1418
Blue GCs (sample BV)								Red GCs (sample RV)						
1	2.15	243	30	35	1.44	2.73	1439	1.89	248	30	35	1.12	2.19	1456
2	3.15	357	47	35	2.75	3.75	1346	2.49	287	35	35	2.20	2.82	1451
3	4.49	304	37	35	3.76	4.94	1470	3.20	286	38	35	2.83	3.74	1363
4	5.57	333	41	35	4.98	5.95	1473	4.22	306	47	35	3.76	4.66	1577
5	6.46	408	50	35	6.03	6.93	1386	5.04	228	28	35	4.67	5.45	1422
6	7.68	314	39	35	6.96	8.71	1419	5.94	259	34	35	5.46	6.44	1502
7	9.76	306	37	35	8.80	10.93	1452	7.04	225	28	35	6.54	7.63	1404
8	11.70	267	35	35	10.94	12.84	1375	8.84	223	28	35	7.69	10.68	1447
9	15.32	301	37	35	12.87	20.88	1419	14.21	196	21	49	10.69	29.19	1449
10	29.20	204	32	21	21.16	41.66	1416							

Notes. The dispersion profiles are obtained using a moving bin of 35 GCs. The bins do not overlap, and the minimum number of GCs per bin was set to 20, hence the large number of GCs in the last bin of sample RV. For each bin, $\bar{R}$ is the mean radial distance from NGC 1399, and $R_{\rm min}$ and $R_{\rm max}$ give the radial range covered by the GCs of the bin (at a distance of 19 Mpc, 1′.0 corresponds to 5.52 kpc). $N_{\rm GC}$ is the number of GCs in a given bin. The line-of-sight velocity dispersion σ and its uncertainty $\Delta\sigma$ are calculated using the estimator by Pryor & Meylan (1993). The asterisk marks the data point which was omitted when modelling the sample RIII.

References

Abramowitz, M., & Stegun, I. A. 1964, Handbook of Mathematical Functions with Formulas, Graphs, and Mathematical Tables, ninth dover printing, tenth gpo printing edn. (New York: Dover)
Ashman, K. M., & Zepf, S. E. 1992, ApJ, 384, 50
Avni, Y. 1976, ApJ, 210, 642
Bassino, L. P., Faifer, F. R., Forte, J. C., et al. 2006, A&A, 451, 789 (B+06)
Baum, W. A. 1955, PASP, 67, 328
Beasley, M. A., Baugh, C. M., Forbes, D. A., Sharples, R. M., & Frenk, C. S. 2002, MNRAS, 333, 383
Bedin, L. R., Piotto, G., Anderson, J., et al. 2004, ApJ, 605, L125
Bekki, K., Beasley, M. A., Brodie, J. P., & Forbes, D. A. 2005, MNRAS, 363, 1211
Bekki, K., Forbes, D. A., Beasley, M. A., & Couch, W. J. 2003, MNRAS, 344, 1334
Bellazzini, M., Ferraro, F. R., & Ibata, R. 2003, AJ, 125, 188
Bergond, G., Athanassoula, E., Leon, S., et al. 2007, A&A, 464, L21 (B+07)
Blakeslee, J. P., Tonry, J. L., & Metzger, M. R. 1997, AJ, 114, 482
Brodie, J. P., & Strader, J. 2006, ARA&A, 44, 193
Bullock, J. S., Kolatt, T. S., Sigad, Y., et al. 2001, MNRAS, 321, 559
Burkert, A. 1995, ApJ, 447, L25
Côté, P., McLaughlin, D. E., Hanes, D. A., et al. 2001, ApJ, 559, 828
Côté, P., McLaughlin, D. E., Cohen, J. G., & Blakeslee, J. P. 2003, ApJ, 591, 850
Catelan, M. 2009, Ap&SS, 18
Churazov, E., Forman, W., Vikhlinin, A., et al. 2008, MNRAS, 388, 1062
Cohen, J. G., Blakeslee, J. P., & Ryzhov, A. 1998, ApJ, 496, 808
Cohen, J. G., Blakeslee, J. P., & Côté, P. 2003, ApJ, 592, 866
Cohen, J. G., & Ryzhov, A. 1997, ApJ, 486, 230
Colavitti, E., Pipino, A., & Matteucci, F. 2009, A&A, 499, 409
Collins, C. A., Stott, J. P., Hilton, M., et al. 2009, Nature, 458, 603
Côté, P. 1999, AJ, 118, 406
Côté, P., Marzke, R. O., & West, M. J. 1998, ApJ, 501, 554
Côté, P., West, M. J., & Marzke, R. O. 2002, ApJ, 567, 853
D'Agostino, R. B., & Stephens, M. A. 1986, Goodness-of-fit techniques (New York, NY, USA: Marcel Dekker, Inc.)
di Matteo, P., Bournaud, F., Martig, M., et al. 2008, A&A, 492, 31
Diemand, J., Zemp, M., Moore, B., Stadel, J., & Carollo, C. M. 2005, MNRAS, 364, 665
Dirsch, B., Richtler, T., Geisler, D., et al. 2003, AJ, 125, 1908 (D+03)
Dirsch, B., Richtler, T., Geisler, D., et al. 2004, AJ, 127, 2114 (D+04)
Drinkwater, M. J., Gregg, M. D., Holman, B. A., & Brown, M. J. I. 2001, MNRAS, 326, 1076
Evans, N. W., Wilkinson, M. I., Perrett, K. M., & Bridges, T. J. 2003, ApJ, 583, 752
Fabricant, D., Lecar, M., & Gorenstein, P. 1980, ApJ, 241, 552
Ferguson, H. C. 1989, AJ, 98, 367
Ferguson, H. C., & Sandage, A. 1989, ApJ, 346, L53
Forbes, D. A., Brodie, J. P., & Grillmair, C. J. 1997, AJ, 113, 1652
Forbes, D. A., Grillmair, C. J., Williger, G. M., Elson, R. A. W., & Brodie, J. P. 1998, MNRAS, 293, 325
Forbes, D. A., Beasley, M. A., Brodie, J. P., & Kissler-Patig, M. 2001a, ApJ, 563, L143
Forbes, D. A., Georgakakis, A. E., & Brodie, J. P. 2001b, MNRAS, 325, 1431
Gebhardt, K., Lauer, T. R., Pinkney, J., et al. 2007, ApJ, 671, 1321
Gentile, G., Salucci, P., Klein, U., & Granato, G. L. 2007, MNRAS, 375, 199
Grillmair, C. J., Freeman, K. C., Bicknell, G. V., et al. 1994, ApJ, 422, L9
Harris, W. E., & Racine, R. 1979, ARA&A, 17, 241
Heisler, J., Tremaine, S., & Bahcall, J. N. 1985, ApJ, 298, 8
Helmi, A. 2008, A&ARv, 15, 145
Hempel, M., Kissler-Patig, M., Puzia, T. H., & Hilker, M. 2007, A&A, 463, 493
Hilker, M., & Richtler, T. 2000, A&A, 362, 895
Hilker, M., Infante, L., & Richtler, T. 1999, A&AS, 138, 55
Hilker, M., Kayser, A., Richtler, T., & Willemsen, P. 2004, A&A, 422, L9
Hou, A., Parker, L. C., Harris, W. E., & Wilman, D. J. 2009, ApJ, 702, 1199
Huchra, J., & Brodie, J. 1987, AJ, 93, 779
Ihaka, R., & Gentleman, R. 1996, J. Comput. Graph. Stat., 5, 299
Ibata, R., Irwin, M., Lewis, G. F., & Stolte, A. 2001, ApJ, 547, L133
Ikebe, Y., Ezawa, H., Fukazawa, Y., et al. 1996, Nature, 379, 427
Jones, C., Stern, C., Forman, W., et al. 1997, ApJ, 482, 143
Kelson, D. D., Zabludoff, A. I., Williams, K. A., et al. 2002, ApJ, 576, 720
Kissler-Patig, M., Richtler, T., Storm, J., & della Valle, M. 1997, A&A, 327, 503
Kissler-Patig, M., Brodie, J. P., Schroder, L. L., et al. 1998, AJ, 115, 105
Kundu, A., & Whitmore, B. C. 2001a, AJ, 121, 2950
Kundu, A., & Whitmore, B. C. 2001b, AJ, 122, 1251
Kundu, A., Zepf, S. E., Hempel, M., et al. 2005, ApJ, 634, L41
Larsen, S. S., & Richtler, T. 2000, A&A, 354, 836

Larsen, S. S., Brodie, J. P., Huchra, J. P., Forbes, D. A., & Grillmair, C. J. 2001, AJ, 121, 2974
Lee, Y.-W., Gim, H. B., & Casetti-Dinescu, D. I. 2007, ApJ, 661, L49
Machacek, M., Dosaj, A., Forman, W., et al. 2005, ApJ, 621, 663
Makishima, K., Ezawa, H., Fukuzawa, Y., et al. 2001, PASJ, 53, 401
Mamon, G. A., & Łokas, E. L. 2005, MNRAS, 363, 705
Mihos, J. C., & Hernquist, L. 1996, ApJ, 464, 641
Minniti, D., Kissler-Patig, M., Goudfrooij, P., & Meylan, G. 1998, AJ, 115, 121
Navarro, J. F., Frenk, C. S., & White, S. D. M. 1997, ApJ, 490, 493
Paolillo, M., Fabbiano, G., Peres, G., & Kim, D.-W. 2002, ApJ, 565, 883
Peng, E. W., Ford, H. C., & Freeman, K. C. 2004, ApJS, 150, 367
Peng, E. W., Jordán, A., Côté, P., et al. 2006, ApJ, 639, 95
Perea, J., del Olmo, A., & Moles, M. 1990, A&A, 237, 319
Pipino, A., D'Ercole, A., & Matteucci, F. 2008, A&A, 484, 679
Press, W. H., Flannery, B. P., Teukolsky, S. A., & Vetterling, W. T. 1992, Numerical Recipes in C: The Art of Scientific Computing (Cambridge University Press)
Pryor, C., & Meylan, G. 1993, in Structure and Dynamics of Globular Clusters, ASP Conf. Ser., 50, 357
Racine, R. 1968, JRASC, 62, 367
Renzini, A. 2006, ARA&A, 44, 141
Richtler, T. 2006, Bull. Astr. Soc. India, 34, 83
Richtler, T., Dirsch, B., Gebhardt, K., et al. 2004, AJ, 127, 2094 (Paper I)
Richtler, T., Grebel, E. K., Domgoergen, H., Hilker, M., & Kissler, M. 1992, A&A, 264, 25
Richtler, T., Schuberth, Y., Hilker, M., et al. 2008, A&A, 478, L23
Romanowsky, A. J., Strader, J., Spitler, L. R., et al. 2009, AJ, 137, 4956
Royston, P. 1982, Applied Statistics, 115
Saglia, R. P., Kronawitter, A., Gerhard, O., & Bender, R. 2000, AJ, 119, 153
Saha, P., Bicknell, G. V., & McGregor, P. J. 1996, ApJ, 467, 636
Schuberth, Y., Richtler, T., Dirsch, B., et al. 2006, A&A, 459, 391
Schuberth, Y., Richtler, T., Bassino, L., & Hilker, M. 2008, A&A, 477, L9
Schweizer, F. 2006, in Globular clusters-Guide to Galaxies, ed. T. Richtler, & S. Larsen (Berlin, Heidelberg: Springer), 2009 [arXiv:astro-ph/0606036]
Schweizer, F., & Seitzer, P. 1993, ApJ, 417, L29
Shapiro, S. S., & Wilk, M. B. 1965, Biometrika, 3
Spitler, L. R., Forbes, D. A., Strader, J., Brodie, J. P., & Gallagher, J. S. 2008, MNRAS, 385, 361
Stephens, M. A. 1974, J. American Statistical Association, 69, 730
Tal, T., van Dokkum, P. G., Nelan, J., & Bezanson, R. 2009, AJ, 138, 1417
Tonry, J., & Davis, M. 1979, AJ, 84, 1511
Toomre, A. 1977, in Evolution of Galaxies and Stellar Populations, ed. B. M. Tinsley, & R. B. Larson, 401
Trager, S. C., Faber, S. M., Worthey, G., & González, J. J. 2000, AJ, 120, 165
van der Marel, R. P., & Franx, M. 1993, ApJ, 407, 525
Venables, W. N., & Ripley, B. D. 2002, Modern Applied Statistics with S, 4th edn. (New York: Springer)
Villanova, S., Piotto, G., King, I. R., et al. 2007, ApJ, 663, 296
Wang, Z., Fazio, G. G., Ashby, M. L. N., et al. 2004, ApJS, 154, 193
Weidner, C., Kroupa, P., & Larsen, S. S. 2004, MNRAS, 350, 1503
Weijmans, A.-M., Krajnović, D., van de Ven, G., et al. 2008, MNRAS, 383, 1343
Whitmore, B. C., & Schweizer, F. 1995, AJ, 109, 960
Woodley, K. A., Harris, W. E., Beasley, M. A., et al. 2007, AJ, 134, 494
Yoon, S.-J., Yi, S. K., & Lee, Y.-W. 2006, Science, 311, 1129
Zinn, R. 1985, ApJ, 293, 424